EVALUATION OF ADVANCED HVAC SYSTEMS EQUIPPED WITH THERMAL ENERGY STORAGE AND BOOSTER FANS

BEHDAD REZANEJADZANJANI

A THESIS SUBMITTED TO THE FACULTY OF GRADUATE STUDIES
IN PARTIAL FULFILLMENT OF THE REQUIREMENTS FOR THE DEGREE OF
MASTER OF APPLIED SCIENCE

GRADUATE PROGRAMME IN MECHANICAL ENGINEERING
YORK UNIVERSITY
TORONTO, ONTARIO

SEPTEMBER 2021

©BEHDAD REZANEJADZANJANI, 2021

ABSTRACT

A major portion of the energy consumed in residential buildings is used for heating, ventilation, and air-conditioning (HVAC) systems. In fact, globally, HVAC systems consume more than 50% of the energy used in buildings. Many HVAC systems do not operate efficiently and lose 25-40% of their cooling or heating energy. Furthermore, considering daily temperature fluctuations, the efficiency of HVAC systems can be improved through the use of thermal energy storage (TES). The focus of this thesis is to investigate the potential to enhance the performance of HVAC systems through the use of fans, dampers, and integrated TES. Low-powered fans placed in vents (booster fans) are investigated for their performance to improve heating and cooling and reduce HVAC system run times. Furthermore, "smart" booster fans and dampers are considered in the simulations by optimizing the times at which they can be turned on or off during the simulations. Results show that the smart booster fan can significantly improve, even by greater than a factor of two, the airflow at a bad vent and the duty cycle of HVAC systems can be reduced to 4.5 hr/day. Duct systems with silica-based TES are also investigated. The silica-based TES system is charged using hot air, coming from a fan equipped with a resistive heater. Thus, the stored thermal energy is generated using electric power, providing an avenue for efficient electrification of heating in buildings. Experimental results show more than 50% of the amount of thermal energy that can be stored in the silica gel can be stored and retrieved as heated air.

ACKNOWLEDGEMENTS

I would like to express my sincere gratitude and appreciation to my supervisor Prof. O'Brien for the continuous support of my master's study and research, for his patience, motivation, enthusiasm, and knowledge. His guidance helped me in all the time of research and writing of this thesis. I could not have imagined having a better supervisor for my master's study. I would like to thank the rest my thesis committee members: Prof. Hanson and Prof. Krol for their encouragement and insightful comments. My sincere thanks also goes to Mr. Kaveh Raeesi for the useful discussions and support. I thank my fellow lab mates especially Kapil Narwal for his huge guidance and support. Last but not the least, I would like to thank my family for supporting me throughout the time I spent on this research, and to those who were close, encouraging me to keep working as hard as I could to finish this thesis.

TABLE OF CONTENTS

LIST OF TABLES

LIST OF FIGURES

List of symbols

Symbol		Units	Symbol		Units
A	Area	m^2	k	The turbulence kinetic energy	$m^2 \cdot s^{-2}$
ρ	Fluid density	$kg \cdot m^{-3}$	ε	Rate of dissipation	$m^2 \cdot s^{-3}$
V	Volume	m^3	E	Energy	J
T	Temperature	K	Re	Reynolds number	
C_p	Specific heat	$J \cdot kg^{-1} \cdot K^{-1}$	G_k	The generation of turbulence kinetic energy due to the mean velocity gradients	$m^2 \cdot s^{-2}$
C	Courant number		G_b	The generation of turbulence kinetic energy due to buoyancy	$m^2 \cdot s^{-2}$
t	Time	s	D_H	Hydraulic diameter	m
p	Static pressure	Pa	σ_k	The turbulent Prandtl numbers for k	
P_w	Wetted perimeter	m	σ_ε	The turbulent Prandtl numbers for ε	
$\bar{\bar{\tau}}$	Stress tensor	$N \cdot m^{-2}$	M_t	The turbulent Mach number	
g	Gravitational acceleration	$N \cdot kg^{-1}$	θ	The fraction of the total available adsorption sites	
K	Adsorption equilibrium constant	mol^{-1}	a	The speed of sound	$m \cdot s^{-1}$
$\vec{F}$	External body forces	N	μ_t	The turbulent (or eddy) viscosity	$m^2 \cdot s^{-1}$
μ	Molecular viscosity	$kg \cdot m^{-1} \cdot s^{-1}$	v	Velocity	$m \cdot s^{-1}$
I	Unit tensor		S_h	Volumetric heat sources	$J \cdot K^{-1} \cdot m^{-3}$
k_{eff}	Effective conductivity	$W \cdot m^{-1} \cdot k^{-1}$	h	Sensible enthalpy	J
k_t	Turbulent thermal conductivity	$W \cdot m^{-1} \cdot k^{-1}$	Y_j	The mass fraction of species j	
$\vec{J}_j$	Diffusion flux of species j	$mol \cdot m^{-2} \cdot s^{-1}$	η_{sc}	Storage capacity efficiency	
			η_{tes}	The TES efficiency	

List of acronyms

HVAC	Heating, ventilation, and air conditioning
TES	Thermal energy storage
CFD	Computational fluid dynamics
HPs	Heat pumps
COP	Coefficient of performance

Chapter 1
Introduction and background

A major portion of the energy consumed in residential buildings is used for heating, ventilation, and air-conditioning (HVAC) systems. In fact, globally, HVAC systems consume more than 50% of the energy used in buildings [1]. Most HVAC systems are powered by natural gas due to the high operating costs of electric-powered HVAC systems [2,3]. Natural gas consumption has a negative impact on global warming, and a total of 39.7 metric tons of CO_2 was emitted by natural gas-powered HVAC systems in Canada alone in 2016 [4,5].

1.1 Introduction and background for the evaluation of smart booster fans and dampers for advanced HVAC systems

Many HVAC systems do not operate efficiently and lose 25 – 40% of their cooling or heating energy. A significant portion of these loses occur through the HVAC systems duct work. Duct systems may lose energy via heat transfer through the duct walls, or air leakage through damaged or poorly connected sections of the ductwork. Further, duct systems may be inefficient if poorly designed or installed, or if they become dirtied or obstructed over their lifetime [6]. Inadequate ducting systems cause high HVAC duty cycles and unnecessary CO_2 emissions. Improving the energy efficiency of HVAC systems has a large effect on reducing the consumption of fossil fuels, which has motivated research towards improving the efficiency of HVAC systems globally [6-9].

In addition to improving the energy efficiency of HVAC systems, it is also important to achieve proper ventilation rates and comfortable conditions to promote a healthy indoor environment [10,11]. Jahantigh et al. [12] studied a hybrid heating set-up comprised of a radiant heater and ventilated airflow in a residential building, in order to decrease the losses of heating energy and fuel consumption. The conditions and flow field surrounding a manikin which is located in the center of a 3*4*4 m^3 room with height of 1.75 m, were simulated to optimize the system parameters. Their results showed that the hybrid heating system can quickly provide thermal comfort in a residential room and can reduce heating losses through walls by up to 25%. In a numerical and experimental study, to solve the air conditioning problem in winters wherein hot air is collected at the top of the room while colder air resides at the bottom, Delavari et al. [13] used a vertical duct with two fans at each end to circulate the air inside the room. Their result showed that the air conditioning duct inside the room could improve the energy efficiency coefficient from 0.43 to 1.05. The energy coefficient shows how much the air conditioning system focuses on the desired area over the undesired area, and if it is greater than one this implies more energy is concentrated in the target area, which results in increased energy savings. Other strategies have focused on sensor-based demand-controlled ventilation [14]. Research directed towards implementing these strategies has focused on CO_2 concentration-based sensors [15], occupant-based sensing [16], and zone temperature-based sensing [17]. In this thesis, the effects of installing smart booster fans and dampers on the ability to regulate airflow and to reduce the duty cycle of a HVAC system within a residential building is investigated. The results from this investigation are presented in Chapter Two.

1.2 Introduction and background for the numerical investigation of heat transfer in air channels for thermal energy storage applications in buildings

Energy demand has significantly increased in building sectors over the past decade because of population growth, increased indoor activities, and more energy required to control the internal environment due to global climate change [18]. In Ontario, about 20% of the total energy supply is consumed in the form of electricity, most of which comes from non-emitting sources such as nuclear and hydro, while the other 80% is derived from burning fossil fuels for heating, transportation, and industry [19]. According to the Internal Energy Agency, in most countries the residential sector accounts for ~30% of the total energy consumption, however in terms of primary energy this value increases to around 40% [20]. Space heating, water heating, and cooking account for most of the fossil fuel use in residential buildings [18]. The energy required for space heating of residential buildings can be decreased by improving insulation, minimizing air leakage, using heat recovery from ventilation air, and optimizing the design of the components that are responsible for heating and cooling such as vents and ducts [21]. An important approach to minimizing energy consumption in the building sector is through life cycle analysis [22]. The life cycle of a building includes the production of building materials, construction, the use phase (which includes operation and maintenance), disassembly, and disposal. All these phases can be considered in order to minimize the life cycle energy use and CO_2 emissions. Several studies have shown that for buildings constructed in temperate or cold regions, most of the energy consumption over the building's life cycle occurs during the use phase [23-25]. Thus, integrating and optimizing the design of HVAC components that reduce energy consumption during the use phase in buildings is a sensible strategy.

In order to improve the efficiency of these systems, several studies have been done to reach the optimal design of heat transfer fins and channels. Each of these studies have suggested various shapes and designs based on their systems [26-28]. In another study, Mohan et al. [29] gave both theoretical and simulation analysis for the duct size. They also compared the pressure loss in rectangular and circular ducts, concluding that the circular duct has minimal friction loss. Also, Shah et al. [30] compared rectangular and circular ducts and showed that rectangular ducts cause more turbulence compared to circular ducts. In the study of the evaluation of smart booster fans and dampers for advanced HVAC systems, a prototype duct system was used to measure and evaluate the ability for smart booster fans and dampers to control airflow to different vents for the purpose of increasing the efficiency of HVAC systems. The results from both the experimental and numerical evaluation show that the smart booster fan and dampers can significantly improve the airflow at a vent that is underperforming [31].

Chapter Three of this thesis discusses the research about the numerical investigation of heat transfer in air channels for thermal energy storage (TES) applications in buildings. In this study the effects of the cross-sectional shape of air-channels on heat transfer from the internal surface of channels to air flowing through the channels is investigated. Air channels with circular, triangular, rectangular and sinusoidal shaped cross sections are considered. Further, heat transfer to air flowing through beds comprising these air channel shapes are also investigated. The beds have a greater cross-sectional area than the channels and can be used in the design of ducts that transport larger volumes of air in HVAC systems. Numerical analyses are performed to investigate the outlet temperatures to optimize the shape of the air channels and beds.

1.3 Simulations

Engineers use computational fluid dynamics (CFD) to analyze and design the best HVAC system before installing or building the actual system or its prototype. CFD helps to understand the different aspects of the flow such as velocity, chemical and thermal reactions and to over come the problems that the HVAC systems might have and find the best solutions. So, it is necessary to conduct a CFD simulation for any HVAC system. There are huge number of applications for HVAC systems that can be simulated by CFD such as designing of the ventilation systems, building rooms or offices temperatures, designing the hood, steam and smoke evacuations, fire simulations, designing the ventilation of swimming pools and so on.

1.3.1 Governing equations

Different equations were used in numerical simulations of flow. In this section, equations are shown:

The mass conservation equation

The conservation of mass equation, or the equation for continuity, is explained below [32]:

$$\frac{\partial \rho}{\partial t} + \nabla \cdot (\rho \vec{v}) = 0 \tag{1-1}$$

where $\vec{v}$ is the velocity, the fluid density is ρ, and time is represented by t.

The momentum conservation equation

Equation 1-2 represents the momentum conservation equation in a fixed frame which does not have any acceleration. [33]:

$$\frac{\partial}{\partial t}(\rho \vec{v}) + \nabla \cdot (\rho \vec{v} \otimes \vec{v}) = -\nabla p + \nabla \cdot (\bar{\bar{\tau}}) + \rho \vec{g} + \vec{F} \tag{1-2}$$

where the static pressure is p, $\bar{\bar{\tau}}$ (described below) is the stress tensor, and $\vec{F}$ and $\rho \vec{g}$ are the external body forces and gravitational body force, respectively.

Below, $\bar{\bar{\tau}}$ (the stress tensor) is shown [33]:

$$\bar{\bar{\tau}} = \mu[(\nabla \cdot \vec{v} + \nabla \cdot \vec{v}^{T}) - \frac{2}{3} \nabla (\vec{v} \cdot \vec{I})] \tag{1-3}$$

where I is the unit tensor, the molecular viscosity is represented by μ, and the effect of volume expansion is shown as the last term on the right side of the equation.

The energy conservation equation

The energy conservation equation is shown below [33]:

$$\frac{\partial}{\partial t}(\rho E) + \nabla \cdot \left(\vec{v}(\rho E + p)\right) = \nabla \cdot \left(k_{eff} \nabla T - \sum_j h_j \vec{J}_j + \left(\bar{\bar{\tau}}_{eff} \cdot \vec{v}\right) \right) + S_h \qquad (1\text{-}4)$$

Where p is the static pressure, ρ is the fluid density, $\vec{v}$ is the velocity, t is the time, k_{eff} is the effective conductivity $(k + k_t)$, where k_t is the turbulent thermal conductivity, and $\vec{J}_j$ is the diffusion flux of species j. $k_{eff} \nabla T$ shows the energy relocation due to conduction, $\sum_j h_j \vec{J}_j$ shows the diffusion of species j, and $\bar{\bar{\tau}}_{eff} \cdot \vec{v}$ shows the viscous dissipation. S_h is the heating sources that are defined by the user, sources such as heat flux from a surface, radiation, and surface temperature.

In equation 1-4 [33]:

$$E = h - \frac{p}{\rho} + \frac{v^2}{2} \qquad (1\text{-}5)$$

Where h represents the sensible enthalpy. The equation of h for ideal gases is described below:

$$h = \sum_j Y_j h_j \qquad (1\text{-}6)$$

In equation 1-6 Y_j is the mass fraction of species j and

$$h_j = \int_{T_{ref}}^{T} C_{p,j} dT \qquad (1\text{-}7)$$

Where T_{ref} is 298.15 K, and $C_{p,j}$ represents the specific heat of species j at a constant pressure.

Standard k-ε model

The sizes of large-scale eddies at the inlet in a CFD simulation of turbulent flow are defined using the turbulent length scale, also the time scale of eddies is calculated using the viscosity and dissipation. Both turbulent length and time scale are calculated by two-equation turbulence models. These models calculate two equations to measure the turbulent length and time scale. Ansys Fluent standard k-ε model, a semi-empirical model which solves the equations of model transport for dissipation rate (ε), and turbulence kinetic energy (k) is one such turbulence model and is economic, robust, and accurate for industrial-grade heat and flow simulations. The extraction of the model equations depends on the boundary conditions and empiricism. Turbulence kinetic energy (k) is derived from an exact equation while the dissipation rate (ε) is obtained using physical reasoning. The standard k-ε model [34] is valid only for fully turbulent flow and neglects molecular level viscosity. Many modified variants are developed to implement this model over a wide range of flow conditions. Two such model implementations are the RNG-model [35] and the realizable k-ε model [36]. The rate of dissipation, ε, and turbulence kinetic energy, k, are calculated from Equations 1-8 and 1-9:

$$\frac{\partial}{\partial t}(\rho k) + \frac{\partial}{\partial x_i}(\rho k u_i) = \frac{\partial}{\partial x_j}\left[\left(\mu + \frac{\mu_t}{\sigma_k}\right)\frac{\partial k}{\partial x_j}\right] + G_k + G_b - \rho\varepsilon - Y_M + S_k \qquad (1\text{-}8)$$

And

$$\frac{\partial}{\partial t}(\rho\varepsilon)+\frac{\partial}{\partial x_i}(\rho\varepsilon u_i)=\frac{\partial}{\partial x_j}\left[\left(\mu+\frac{\mu_t}{\sigma_\varepsilon}\right)\frac{\partial\varepsilon}{\partial x_j}\right]+C_{1\varepsilon}\frac{\varepsilon}{k}(G_k+C_{3\varepsilon}G_b)-C_{2\varepsilon}\rho\frac{\varepsilon^2}{k}+S_\varepsilon \quad (1\text{-}9)$$

G_k is the turbulence kinetic energy generation regarding the mean velocity gradients, shown in 1-10. G_b represents the turbulence kinetic energy generation as a result of buoyancy, calculated in 1-11. Y_M shows the participation of the fluctuating expansion in compressible turbulence to the average dissipation rate, shown in 1-13. $C_{1\varepsilon}$, $C_{2\varepsilon}$, and $C_{3\varepsilon}$ are constants. σ_ε and σ_k are the turbulent Prandtl numbers for ε and k, respectively. S_k and S_ε are turbulence and heating sources, respectively, which are defined by the user.

$$G_k=-\rho\overline{\acute{u}_i\acute{u}_j}\frac{\partial u_j}{\partial x_i} \quad (1\text{-}10)$$

$$G_b=\beta g_i\frac{\mu_t}{Pr_t}\frac{\partial T}{\partial x_i} \quad (1\text{-}11)$$

Where $\acute{u}_i$ and $\acute{u}_j$ represent the fluctuating velocities in the corresponding direction. The turbulent Prandtl number is Pr_t for energy and g_i is the gravitational vector in the i^th direction. β is the coefficient of thermal expansion, calculated as 1-12:

$$\beta=-\frac{1}{\rho}\left(\frac{\partial\rho}{\partial T}\right)_p \quad (1\text{-}12)$$

$$Y_M=2\rho\varepsilon {M_t}^2 \quad (1\text{-}13)$$

where the turbulent Mach number, M_t is shown as:

$$M_t=\sqrt{\frac{k}{a^2}} \quad (1\text{-}14)$$

Where a is the velocity of sound.

The turbulent viscosity (or eddy viscosity), μ_t , is calculated as below:

$$\mu_t = \rho C_\mu \frac{k^2}{\varepsilon} \tag{1-15}$$

Where C_μ is a constant.

$C_{1\varepsilon}$, $C_{2\varepsilon}$, C_μ, σ_k and, σ_ε are constant numbers given as [34]:

$$C_{1\varepsilon} = 1.44, C_{2\varepsilon} = 1.92, C_\mu = 0.09, \sigma_k = 1.0, \sigma_\varepsilon = 1.3 \tag{1-16}$$

In order to predict the pattern of the fluid, the Reynolds number should be calculated for each study as follows:

$$Re = \frac{\rho u D_H}{\mu} \tag{1-17}$$

Where the ρ is the density of the fluid, u is the mean velocity, D_H is the hydraulic diameter, and the dynamic viscosity of the fluid is μ.

$$D_H = \frac{4A}{P_w} \tag{1-18}$$

Where A represents the cross-sectional area and P_w is the wetted perimeter.

The turbulence model is used in the simulations conducted in Chapter Two.

In order to calculate the time step the Courant number, which is given by Equation 1-19, is set equal to one.

$$C = \frac{v\Delta t}{\Delta x} \tag{1-19}$$

Where v is the flow velocity, Δt is the time step, and Δx is the grid spacing.

1.4 Introduction and background for the application of adsorption-based thermal energy storage in HVAC systems

1.4.1 Background of decarbonized electricity and heat pumps in the building sector

Decarbonization of electricity generation followed by electrification in the buildings sector is known to be one of the promising pathways to achieve a low carbon future [37]. It is estimated that eliminating the use of fossil fuels in the building sector can support reductions in CO_2 emissions by 31% by 2050 [38]. There are currently four technologies for electrification of space heating: air source heat pumps (HPs), air source HPs in conjunction with other heating sources, ground source HPs, and electric resistance thermal storage heating. Air source HPs are a common technology used to transport heat from outdoor to interior space during the heating season and from indoors to outdoors during the cooling season. HPs can be ducted or ductless. Ground source HPs transfer the heat to and from earth instead of the outside air. Electric resistance storage heaters, mostly in the form of elements encased in heat storing ceramic, have been used for decades [39]. HPs can produce equivalent space heating for as little as one-quarter the cost of conventional heating or cooling which operate based on fossil fuels [40]. TES systems are mainly used to merge renewable energy in the electricity production mix, and also proved to be useful for storing the electrical energy from peak to off peak hours, becoming useful for demand-side management (DSM) [41].

Using simple heat storage including tanks for the stratified storage of hot and cold water have been studied widely in building applications [42-44]. Sarbu et al. [45] reviewed TES technologies and described several energy storage methods and the calculation of storage capacities such as sensible, latent, and thermo-chemical heat storages. In another study, Patteeuw et al. [46] have coupled TES systems to electric heating systems (HPs and resistance heaters). They showed that only these integrated systems can overcome the constraints on both the supply and demand side of electric power systems. Arteconi et al. [41] analyzed HPs with radiators coupled with TES to show how the HP system operates and affects the thermal comfort of occupants based on demand side management (DSM). They showed that the HPs integrated with TES systems can achieve good control of the indoor temperature, even after three hours of turning off the HPs.

1.4.2 Thermal energy storage

In order to improve renewable energy, much research has been done on energy storage systems. TES systems can conserve and save energy in a storage medium in order to use that energy at a later time [47]. Thermal energy can be stored in various forms: sensible heat, latent heat, and thermochemical heat [48]. Sensible thermal energy (temperature changes when heat is exchanged) technologies utilize the high heat capacity materials in solid, liquid or a mixture of solid and liquid states to store thermal energy. Most materials absorb or release thermal energy while changing the physical phase such as converting from solid phase to liquid phase and vise versa or from liquid phase to gas. Latent thermal energy technologies have this property of changing phases to store thermal energy. Thermochemical energy storage technologies utilize the properties of materials to undergo thermo-chemical reactions after absorbing or releasing thermal energy to store thermal energy. These technologies, apart from heat transfer, also include mass transfer and kinetics of thermo-chemical activity and are more complex in comparison to sensible and latent TES technologies. The TES systems work in a range of temperatures, power levels and with a variety of heat transfer fluids to suit the applications these are intended for, and therefore offer a huge scope of development in terms of system designs and methods. Thermal energy in these systems can be extracted directly from the storage medium or using a heat transfer fluid. There are a range of heat transfer fluids available to select from depending upon the temperature ranges and applications [49]. Installing TES capabilities in HVAC systems can improve the efficiency of the system and decrease carbon dioxide emissions [50].

1.4.3 Adsorption

Adsorption is an exothermic thermochemical surface process in which adsorbate particles adhere to the adsorbent surface. In the adsorption process the solid material is called the adsorbent and the material that adheres to the solid material (also known as solute) is called the adsorbate [51]. Adsorbents are known as a highly porous materials with a pore surface area range between 100 to 1200 m^2/g [51]. The affinity of an adsorbent are determined by the different molecular properties like dimension, the partial pressure, form, and polarity, and concentration in the fluid, and temperature. Van der Waals forces are responsible for adsorption to happen.

1.4.4 Heat and mass-transfer considerations

The adsorbate molecules must find an empty and available space on the adsorbent surface to be adsorbed. This happens when the adsorbate spreads over the adsorbent and by convection, it detects its position along the pore surface of the adsorbent and then adsorbed on it [51]. The entropy of adsorbate molecules decreases when they are adsorbed on the adsorbent surface. The adsorption process results in the net surface energy decrease at the adsorbent material surface, which is giving it an exothermic character ($\Delta H < 0$). Also, adsorption results in the decrease in the entropy of adsorbate molecules ($\Delta S < 0$) in the adsorbate medium as the freedom to movement of adsorbed molecules decreases. As the adsorption is a spontaneous process, this decreases in enthalpy ($\Delta H < 0$) and entropy ($\Delta S < 0$) results in a negative Gibbs Free Energy ($\Delta G = \Delta H - T\Delta S < 0$).

1.4.5 Regeneration

Regeneration is the process in which adsorbate molecules are desorbed from the adsorbent, such that the adsorbent is prepared to provide heat by adsorbing the adsorbates again. There are different types of regeneration methods such as contacting the adsorbent with a solvent that has a higher attachment for the adsorbate, contacting the adsorbent with gas or liquid that has little or no adsorbate, and increasing the temperature.

1.4.6 Silica gel

Silica gel is made of silicon dioxide, having nanometer-scale voids and pores of out of order tridimensional structure of silicon and oxygen atoms. Silica gel (SiO_2) is famous because of its high specific surface area from 300 to 850 m^2/g. Silica gel is safe, cheap, non-corrosive and is regenerated easily by applying heat at temperatures of 70 °C to 100 °C for about 2 hours [52-53]. The amount of energy which is released when adsorption happens is called the heat of adsorption and for the silica gel-water pair this amount is about 2000-2500 kJ/kg of silica gel.

1.4.7 Background literature: adsorption-based thermal energy storage

Currently, adsorption-based TES systems have received a lot of attention among researchers. One of the most important features of this technology is that it can be coupled with different applications such as refrigeration cycles or HPs.

Kubota et al. [54] have worked on the silica gel adsorption HPs. They have designed a fin-type silica gel tube to enhance the heat and mass transfer of the adsorber. In their results they stated that the cooling enhanced more than two times cooling output per unit absorber. Aristo et al. [55] studied adsorption chillers (ACs) in conjunction with adsorption phenomena which uses adsorbent beads. Based on the results of their analysis, the dynamics is constant regarding the ratio of heat transfer surface area over adsorbent mass which may be utilized for evaluating the measure of adsorption bed-heat exchanger's dynamic perfection the degree of dynamic perfection of an adsorbent bed-heat exchanger unit.

Wang et al. [56] have worked on adsorption HPs which contains tubes for the adsorption in regards of cooling. They have stated that, specific cooling power and the coefficient of performance (COP) can increase up to 85 W/kg adsorbent and 0.5, sequentially. In another study, Zhang et al. [57], provided a numerical and experimental study on the honeycomb structure of an adsorption bed. They coated the silica gel on the sinusoidal fin shape. By passing moist air through the bed, they showed that the outlet temperature could rise by about 30˚C. More applications can be found in the literature [58-59].

The focus of research on silica gel studies has mostly been on the applications of dehumidification of the air and less on the opportunity of using the adsorption heat that can be extracted. A novelty of this thesis is to use the adsorption heat of the adsorption phenomena as TES integrated within an HVAC system, specifically during in heating seasons. The TES adsorption bed can be used in conjunction with the heating source in an HVAC system, and smart booster fans to heat a room that has heating problems over an extended period of time without significant increase to the duty cycle of the HVAC system.

1.5 Overview of the thesis

The objectives of the research carried out in this thesis are as follows:

1) To experimentally measure the effects of installing smart booster fans and dampers on the ability to regulate airflow and to numerically evaluate the extent to which these fans can reduce the duty cycle in HVAC systems.

2) To experimentally measure the efficiency with which thermal energy can be stored in adsorbent-based TES systems directly integrated into HVAC ducts.

To achieve objective one, an underperforming duct branch is built inside the laboratory. The duct has four vents, and an air blow is used to provide airflow. The effects of installing booster fans on the airflow through the vents is measured. The results from the experiments are used in CFD simulations (conducted using ANSYS) to numerically evaluate the effects of using the fans on the HVAC duty cycle in a model residential home.

To achieve objective two, an experimental set up is built wherein a TES unit is directly integrated into an HVAC duct branch. This TES unit uses silica-based materials to provide thermochemical energy storage. Hot air is used to “charge” the silica gel. The silica is left to cool to room temperature and thermal energy is subsequently retrieved by flowing humid air across the silica. Experimental results are used to measure the amount and efficiency with which thermal energy is stored and the benefits of using “clean” excess electric power to charge the TES medium is evaluated. The contents of each chapter are described in the following paragraphs.

In Chapter Two, the evaluation of smart booster fans and dampers for advanced HVAC systems are presented. At the beginning an introduction is given about the study then in the materials and methods section the two main parts of this study, which are the experimental and simulation parts, are explained in detail. After this section, the results and conclusions are presented. Results show that the smart booster fan can significantly improve, even by greater than a factor of two, the airflow to a vent at the end of a long duct-branch. These results were also considered in the experiments of the TES bed and ducting system in Chapter Four. In these experiments a booster fan is installed at the end of a duct that is equipped with thermal energy storage to improve airflow and reach the desired velocity. This chapter has been published in the Journal of Green Building and permission to use the article in this thesis has been granted. Chapter Three is about the numerical investigation of heat transfer in air channels for TES applications in buildings. An introduction is given about the study. In the materials and methods, the details of two numerical studies for determining heat transfer within channels and beds are presented. The results shown that sinusoidal beds can assist in the design of the TES bed by applying the adsorbate material on the surface of sinusoidal fins. These results were used to design the TES bed used to carry out the experiments in Chapter Four.

Chapter Four is about the application of adsorption-based TES in HVAC systems. An experimental set up is built wherein a TES unit is directly integrated into an HVAC duct branch. This TES unit uses silica-based materials to provide thermochemical energy storage. Hot air is used to charge the silica gel. The silica is left to cool to room temperature and thermal energy is subsequently retrieved by flowing humid air across the silica. Experimental results are used to measure the amount and thermal energy efficiency with which thermal energy is stored and the benefits of using clean excess electric power to charge the TES medium is evaluated.

Chapter Five presents the conclusions that are obtained from each chapter and also provides recommendations for future work.

Chapter 2
Evaluation of smart booster fans and dampers for advanced HVAC systems

2.1 Introduction

In this work, the effects of installing smart booster fans and dampers on the ability to regulate airflow and to reduce the duty cycle of a HVAC system within a residential building is investigated. A smart booster fan fits in the vents within a residential home, operating on low power (~2 W) to augment HVAC systems and improve their performance. A set of smart booster fans installed in vents throughout a home can measure their local temperature and, through wireless communication, operate in concert to optimize airflow to efficiently achieve the desired temperature at different zones throughout a home. Further, smart dampers installed in certain vents within a home may prevent airflow to preserve conditioned airflow for other vents further along the duct-branch. Herein booster fans and dampers were installed in an experimental prototype of a duct-branch system. The airflows at the inlets throughout this ducting system were measured for different cases wherein fans and dampers were situated at certain inlets within the duct-branch. The results from these experiments were used to numerically model the ability of the smart booster fans and dampers to improve airflow, regulate temperature, and reduce energy consumption, with a focus on underperforming inlets at the end of a long duct-branch in a model residential house.

2.2 Materials and methods

2.2.1 Experimental measurements

A duct-branch within a HVAC system was simulated inside the laboratory by designing and building a duct system equipped with an air blower that could be used to perform experiments. Images of the designed and actual experimental set-up are shown in Figures 2.1a and 2.1b, respectively. The duct-branch distributes air to four registers, or vents, and is enfolded in a wooden enclosure of size 120 x 233 x 60 cm^3. Flexible ducting made of Aluminum was used. An air blower brings air in through an intake at the bottom left corner of the apparatus. The length of the duct between the blower and the first duct exit boot (vent 1) is 2 m. The duct between the blower and vent 1 has an 8” diameter, while all other ducts in the apparatus have a 4” diameter. The length of ducting from the blower to the second, third and fourth vents is 5 m, 10.6 m and 19.2 m, respectively. The selection of these duct lengths was based on discussions with engineers from the company that supplied the smart booster fans, which was Smart Cocoon, Inc. The typical duct length for the first vent that goes to the first room is 3 to 6 m, for the second and third vents that go to the second room are 6 to 9 m, and for the fourth vent that goes to third room is 9 to 15 m. The total equivalent length of this ducting system, including additional friction losses due to the curvature of the ducts, is 53.9 m which is comparable with the total equivalent length of some duct-branches in a typical residential unit.

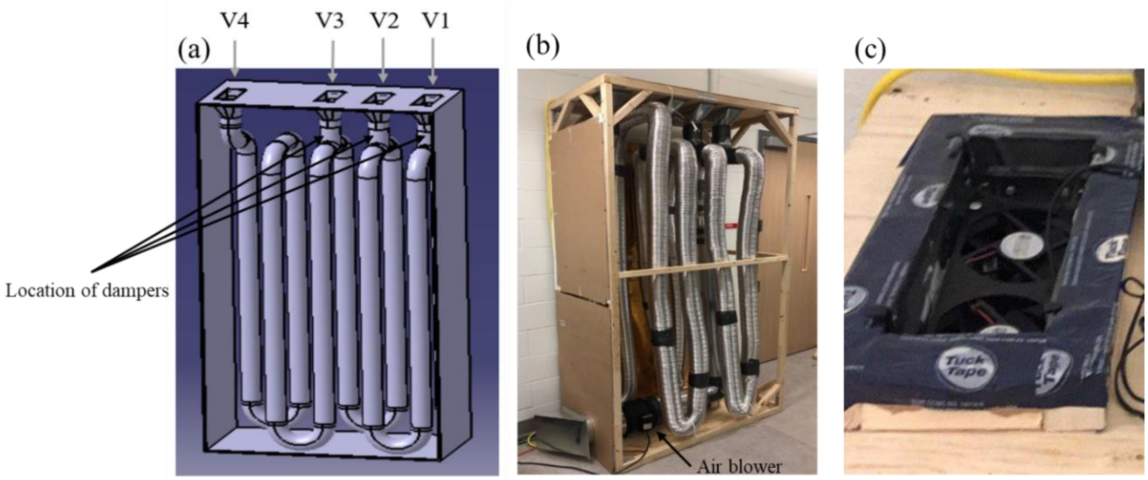

Figure 2.1. (a) Experiment design of duct system (V stands for vent) (b) Experiment duct system (c) Installation of smart booster fan at the vent.

Experiments were performed wherein smart booster fans were placed within different vents in the testing apparatus to determine their effect on air flow rates through the vents. By placing a smart booster fan in the vents which is connected to a smart phone, low airflow rates within the vents can be boosted to cool or heat the room much faster. A Vivosun blower with a maximum flow rate of 0.17 m^3/s (360 CFM) was used to simulate the airflow from a house heater fan. An Extech SDL300 Metal Vane Thermo-Anemometer/Data logger was used to record the flow rates during the experiments. Dampers were installed at the boot of vents 1 and 2, to set the air flow through the duct system. The position of the dampers was set such that the air flow through vent 1, 2, and 3 was 0.042, 0.028, and 0.026 m^3/s (90, 59.3 and 55.6 CFM), respectively. Four experiments were conducted to measure the airflow rates through the four vents along the duct-branch. In the first experiment, no fans or dampers were used. In the second experiment dampers were used at vents 1 and 2 to achieve the desired airflow rates through inlets 1, 2 and 3. In the third experiment the dampers were kept in inlets 1 and 2 and a smart booster fan was used at Inlet 4. The fourth experiment was similar to the third, but with the addition of a second smart booster fan at Inlet 3. The operating conditions for the four experiments are summarized in Table 2.1.

Table 2.1. Operating conditions for experiments one through four.

Experiment No.	Inlet 1		Inlet 2		Inlet 3		Inlet 4	
	Fan	Damper	Fan	Damper	Fan	Damper	Fan	Damper
1	x	x	x	x	x	x	x	x
2	x	✓	x	✓	x	x	x	x
3	x	✓	x	✓	x	x	✓	x
4	x	✓	x	✓	✓	x	✓	x

2.2.2 Numerical simulations

2.2.2.1 Methods used for evaluating the ability of smart booster fans to improve airflow and heating

The data attained from the experimental measurements were used to numerically model the ability of the smart booster fans to improve airflow and heating in a residential house. Numerical analyses were performed assuming an initial indoor temperature of 20 °C, and three different cases were considered wherein the outdoor temperature was 5 °C, 0 °C and -10 °C. CFD analysis was performed using Ansys software. The modelled house has three rooms of sizes 3*3*3 m^3 (9.85*9.85*9.85 ft^3), 3*6*3 m^3 (9.85*19.69*9.85 ft^3) and 3*3*3 m^3 (9.85*9.85*9.85 ft^3), which are referred to as room 1, room 2 and room 3, respectively. All the walls are considered to have a thickness of 0.3 m. The front, left side, and right-side walls of each room are assumed to be exterior walls with a heat transfer coefficient of 1.81 $W/m^2 \cdot K$. This is typical of a wall made of solid brick with plaster on it. The roof, bottom and back walls are assumed to be interior walls that are perfectly insulated with a heat transfer of 0 $W/m^2 \cdot K$. Rooms 1 and 3 have one inlet and one outlet, and room 2 has two inlets and two outlets, all of size 10.16*25.4 cm^2 (4*10 in^2). The model is meshed with 82825 tetrahedral elements with an element size of 0.39 m having a growth rate of 1.20, skewness of 0.84 and aspect ratio of 1.18, as shown in Figure 2.2.a. A diagram of the model house used for the analysis is provided in Figure 2.2.b. The next step is to choose the solver, models, and solution methods that will be used to carry out the numerical simulations. The pressure-based solver type is chosen. In this method, a pressure equation solves the restriction of continuity (also known as the mass conservation) of the velocity. Also, absolute velocity formulation is used to decrease the numerical diffusion and have a more precise solution. The gravitational constant is set to 9.81 $N \cdot kg^{-1}$. To calculate the heat transfer equations, the energy model is selected. Considering the properties of air at 20°C, such as its density (1.2047 $kg \cdot m^3$) and dynamic viscosity (1.8205*10^{-5} $kg \cdot m^{-1} \cdot s^{-1}$), a standard k-e turbulent model is chosen (see Chapter One for details). In the solution methods, the least squares cell based is selected for the gradient, second order is selected for the pressure, second order upwind method is used for the momentum and energy conservation equations, first order upwind is selected for the turbulent kinetic energy and dissipation rate equations, and first order implicit transient formulation is chosen. Subsequently, the hybrid initialization is used to initialize the boundary conditions and to set the initial temperature of the fluid to 20 °C. The last step is to choose the time step of the transient equations. It is determined by setting the Courant number equal to one. A time step of 0.02 s is chosen based on the velocity of the flow and grid spacing. To check the dependency of the simulations on the time step simulations were repeated using a time step of 0.01 s. To check the dependency of the simulations on the grid size, simulations were ran using a new mesh with 119,411 elements. Changing the time step to 0.01 and the mesh size to 119,411 changed the results by only 5% and 2%, respectively. A comparison of the results for simulations carried out using a timestep of 0.01 s and 0.02 s is shown in Figures A1 and A2 in the appendix. Also, a comparison of the results for when the mesh size is 119,411 and 82,825 is shown in Figures A3 and A4 in the appendix.

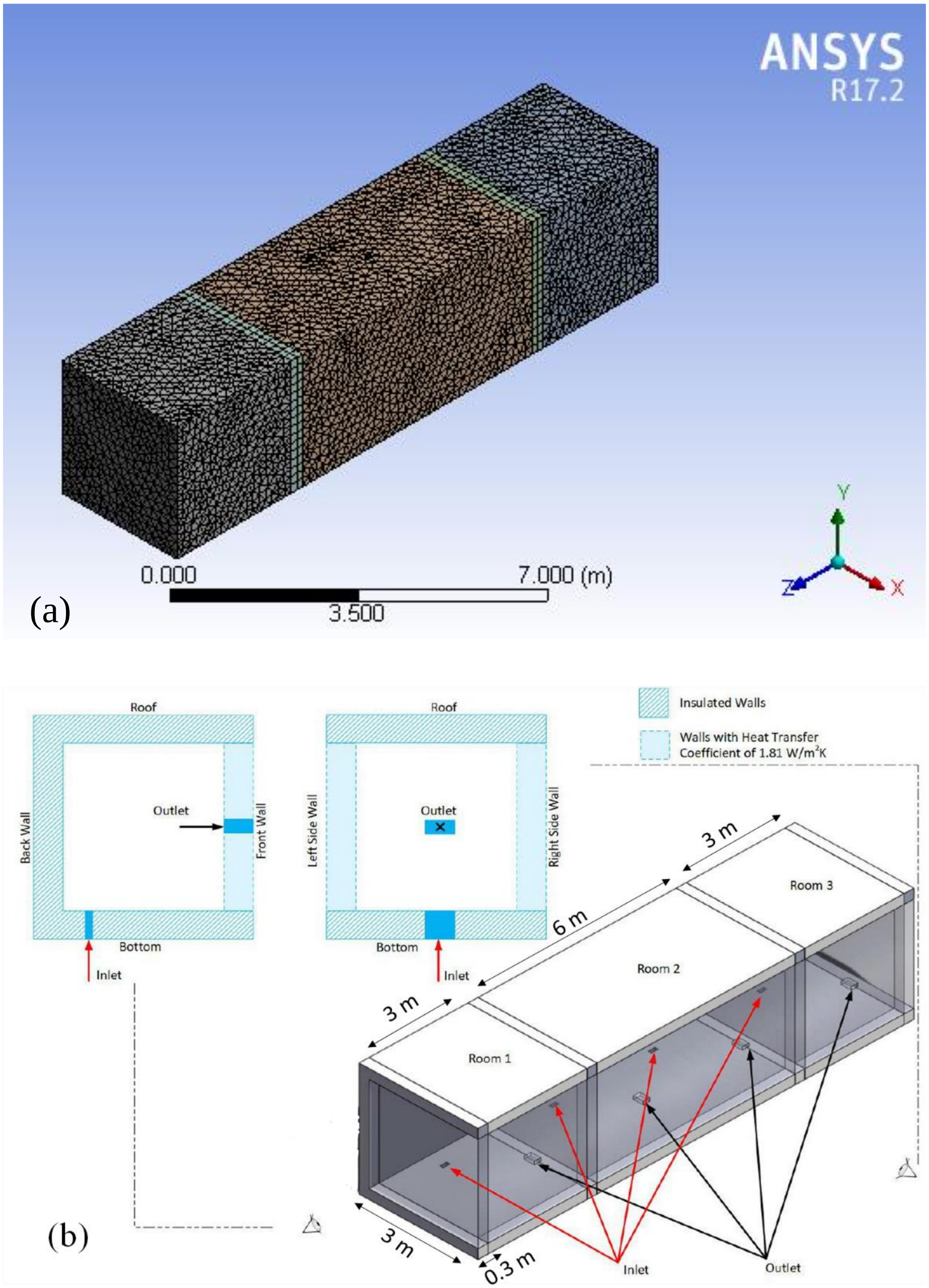

Figure 2.2 (a) House model with specified mesh as modeled in ANSYS (b) Diagram of house model.

The air velocity measurements attained using the ducting apparatus shown in Figure 2.1.b were used as the input velocity at the vents for the CFD simulations. Vent 1 was located in room 1, vents 2 and 3 were located in room 2, and vent 4 was located in room 3. Data used in the simulation is collected from the experiments under ‘with fan’ and ‘without fan’ conditions. The boundary conditions used under ‘with fan’ and ‘without fan’ conditions are as detailed below in Table 2.2:

Table 2.2. The boundary conditions used under ‘with fan’ and ‘without fan’ conditions.

With fan	Inlet 1 (room 1)	Inlet 2 (room 2)	Inlet 3 (room 2)	Inlet 4 (room3)
Airflow m^3/s (CFM)	0.042 (90)	0.028 (59)	0.025 (53)	0.017 (37)

Without fan	Inlet 1 (room 1)	Inlet 2 (room 2)	Inlet 3 (room 2)	Inlet 4 (room3)
Airflow m^3/s (CFM)	0.042 (90)	0.028 (59.3)	0.026 (55.6)	0.008 (17)

Boundary conditions (same for ‘with fan’ and ‘without fan’)	
Inlet airflow temperature (°C)	40 °C
Outlet air pressure (Pa)	1.2 Pa
Insulation walls heat transfer	No heat flux
Wall thickness (m)	0.3 m
Outer walls heat transfer	1.81 $w/m^2 \cdot K$
Initial interior room temperature (°C)	20 °C

2.2.2.2 Methods used for evaluating the ability of smart booster fans and smart dampers to improve airflow and heating

Numerical simulations were performed to investigate the ability of smart booster fans and dampers to regulate the temperature of the building shown in Figure 2.2.b. It is assumed that each room is equipped with its own thermostat and the desired temperature in each room is 22 °C. Further, it is assumed that the HVAC system is turned on and hot air is supplied to the rooms when their temperature drops below 20 °C, and that this hot air supply is not turned off until the temperature of the room reaches 24 °C. Four different cases were considered, and the operating conditions for each case are provided below.

Case 1: There are no fans or dampers present in any of the inlets.

Case 2: Dampers are not present in any of the inlets. A fan is installed in the fourth vent.

Case 3: Fans are not present in any of the inlets. Dampers are installed in inlets 1, 2, and 3.

Case 4: Dampers are installed in all four inlets. A fan is installed in inlet 4.

For cases 1 and 2 the state of the HVAC system is determined by the thermostat in room 3. The HVAC system (airflow) turns on if the temperature in room 3 drops below 20 °C, and turns off if the temperature in this room exceeds 24 °C. For cases 3 and 4 each room has its own thermostat. The HVAC system turns on if the temperature in any room drops below 20 °C and turns off if the temperature in every room is 24 °C or higher. Because the temperature profile of room 1 and room 2 in heating mode are almost the same, the dampers in inlets 1, 2, and 3 are in a closed position when the thermostat in room 1 measures a temperature of 24 °C or higher, such that hot air from the HVAC system is sent exclusively to room 3 via inlet 4. All model designs and boundary conditions are kept as they were in the previous analysis except the airflow at inlets in heating mode which were measured by the experiment and are shown in Table 2.3. For cases 3 and 4 the airflows at the inlets have two stages. In the first stage, which occurs before room 1 reaches 24 °C, all the dampers are in an open position and air flows through all vents. In the second stage, when the temperature of room 1 is at 24 °C or higher, the dampers at inlets 1, 2 and 3 are in a closed position and the airflow at these inlets is zero. Also, the temperature of the airflow at all inlets is assumed to be 45 °C.

Table 2.3. Airflow at inlets for the four different cases considered.

Case 1	Inlet 1 (room 1)	Inlet 2 (room 2)	Inlet 3 (room 2)	Inlet 4 (room3)
Airflow m^3/s (CFM)	0.042 (90)	0.028 (59.3)	0.026 (55.6)	0.008 (17)

Case 2	Inlet 1 (room 1)	Inlet 2 (room 2)	Inlet 3 (room 2)	Inlet 4 (room3)
Airflow m^3/s (CFM)	0.042 (90)	0.028 (59)	0.025 (53)	0.017 (37)

Case 3		Inlet 1 (room 1)	Inlet 2 (room 2)	Inlet 3 (room 2)	Inlet 4 (room 3)
Before room 1 reaches 24°C	Airflow m^3/s (CFM)	0.042 (90)	0.028 (59.3)	0.026 (55.6)	0.008 (17)
After room 1 reaches 24°C	Airflow m^3/s (CFM)	0	0	0	0.040 (85)

Case 4		Inlet 1 (room 1)	Inlet 2 (room 2)	Inlet 3 (room 2)	Inlet 4 (room 3)
Before room 1 reaches 24°C	Airflow m^3/s (CFM)	0.042 (90)	0.028 (59)	0.025 (53)	0.017 (37)
After room 1 reaches 24°C	Airflow m^3/s (CFM)	0	0	0	0.042 (91)

2.3 Results

2.3.1 Experimental results

The results obtained from airflow measurements for experiments one through four are presented in Figures 2.3.a, 2.3.b, and 2.3.c.

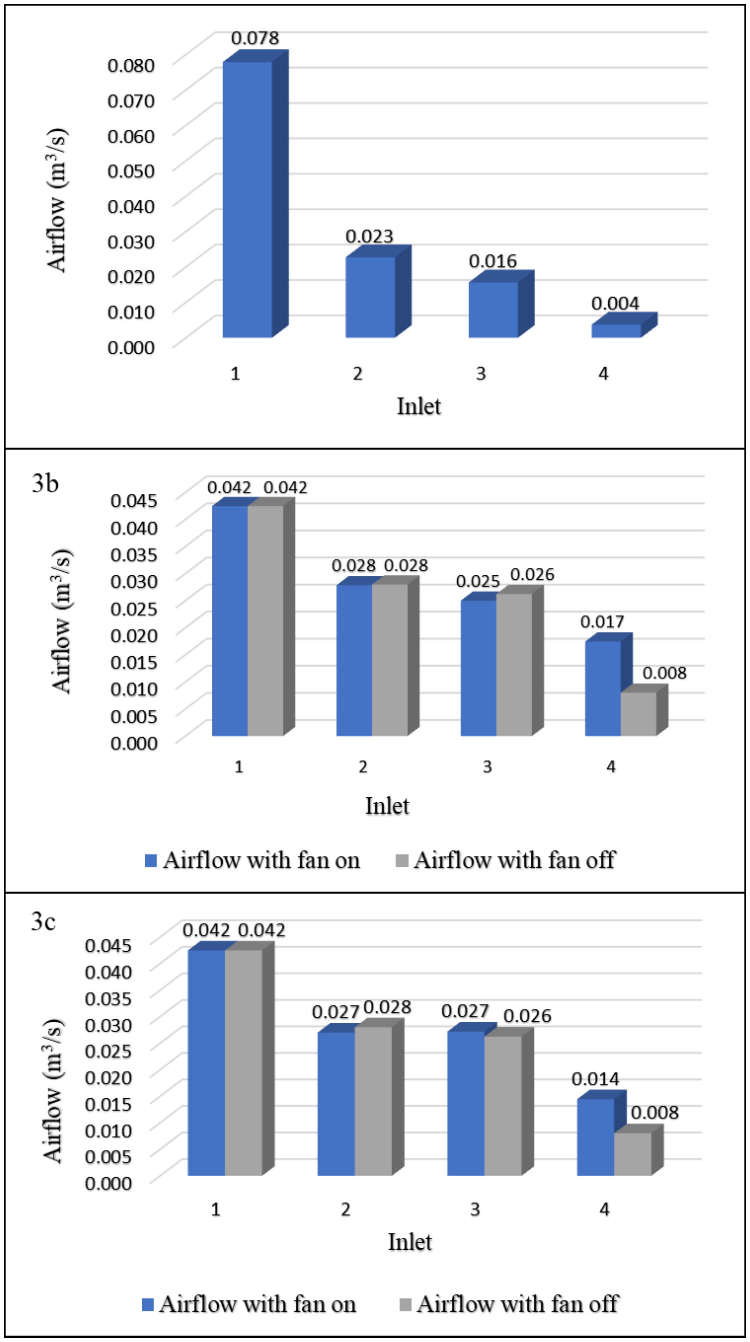

Figure 2.3. (a) Air flow measurements for experiment 1 (no dampers and no fans installed) (b) Air flow measurements for experiment 3 (dampers at vents 1 and 2, one fan installed at vent 4) (c) Air flow measurements for experiment 4 (damper at vents 1 and 2, two fans installed at vent 3 and vent 4).

It is observed from Figure 2.3.b that the airflow through the fourth inlet increases from 0.008 m^3/s (17 CFM) to 0.017 m^3/s (37 CFM) when one fan is installed at the fourth inlet and dampers are positioned at inlets 1 and 2. It can be noted that the overall airflow through all inlets increases by 7.07 %. Furthermore, as shown in Figure 2.3.c, airflow increased from 0.008 m^3/s (17 CFM) to 0.014 m^3/s (30.6 CFM) when smart booster fans are installed at the third and fourth inlets. When smart booster fans are installed at the third and fourth inlets the overall airflow through all inlets increases by 6.03%. Notably, the airflow through the third inlet increased from 0.026 m^3/s (55.6 CFM) to just 0.027 m^3/s (57.6 CFM) when the booster fans were installed at both the third and fourth inlets.

2.3.2 Simulation results

2.3.2.1 Results from evaluating the ability of smart booster fans to improve airflow and heating

Figures 2.4.a to 2.4.f plot the temperature in rooms 1, 2 and 3, for the model residence shown in Figure 2.2.b. The initial temperature for all rooms in the house is 20 °C and the ambient temperature is 5 °C for the results shown in Figures 2.4.a and 2.4.b, 0 °C for the results shown in Figures 2.4.c and 2.4.d, and -10 °C for the results shown in Figures 2.4.e and 2.4.f. The amount of time it takes to heat the rooms from 20 °C to 24 °C with and without a smart booster fan installed within the vent in room 3 is shown for all cases.

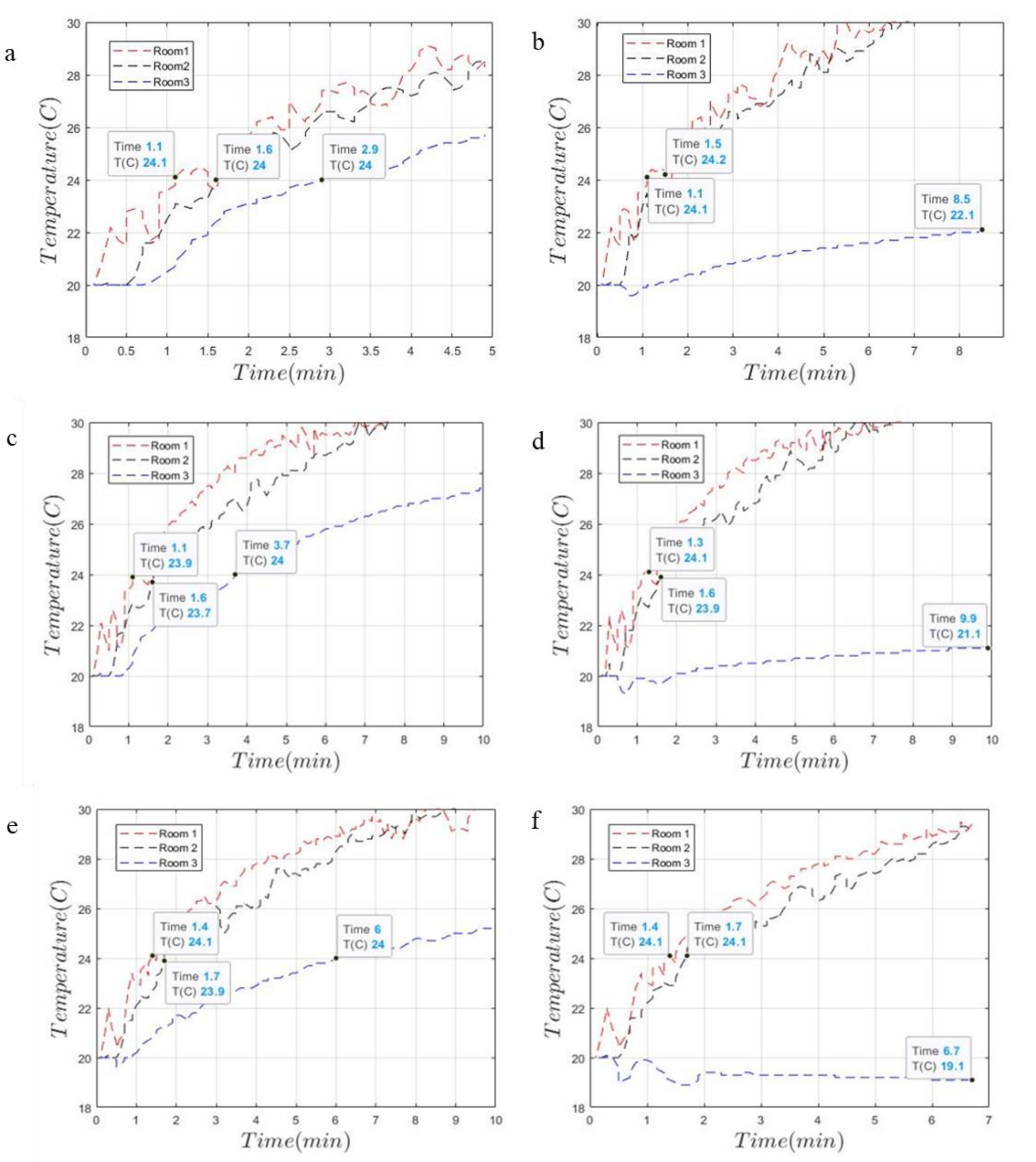

Figure 2.4. (a) Simulation results for an outside temperature of 5 °C with fan, (b) without fan (c) Simulation results for an outside temperature of 0 °C with fan, (d) without fan (e) Simulation results for an outside temperature of -10 °C with fan, (f) without fan.

It is observed from Figure 4 that it would take 2.9 minutes to heat room 3 from 20°C to 24°C with the fan when the outside temperature is 5 °C. However, without a fan installed in room 3 its temperature is just 22.1 °C after 8.5 minutes, and the room will not reach 24 °C in a practical amount of time. When the outside temperature is 0 °C, it would take 3.7 minutes to heat room 3 from 20 °C to 24 °C with the fan installed, but without the fan room 3 does not reach 24 °C (Figure 5). As shown in Figure 6, it would take 6 minutes to heat room 3 from 20 °C to 24 °C with the fan, however, without a fan room 3 is not going to reach 24 °C under an outside temperature of -10 °C. Thus, room 3 will not reach 24 °C in a practical amount of time for any condition considered in this study unless it is equipped with a smart booster fan.

2.3.2.1 Results from evaluating the ability of smart booster fans and smart dampers to improve airflow and heating

Simulations were also performed to study the temperature of the rooms in the model house shown in Figure 2.2.b as the airflow through the vents in the house was turned on and off. In these simulations the airflow through the vents was assumed to be set in an “on” or “off” state based on the temperature reading from a thermostat situated in each room. It is assumed the thermostats in each room is set to 22 °C and the dampers (if installed) would close the inlets of rooms that reaches 24 °C and the airflow would be directed to the other rooms. For these simulations, because of the similarity of the temperature profile in rooms 1 and 2, the dampers in inlets 1, 2, and 3 are in a closed position when the thermostat in room 1 measures a temperature of 24 °C or higher, such that hot air from the HVAC system is sent exclusively to room 3 via inlet 4. The HVAC system turns off when the thermostat in room 3 reaches

24 °C. The system would then remain in the “off” state until the temperature in one of the rooms cools to 20 °C. When the temperature drops to 20 °C, the HVAC system will be turned on until the temperature in room 3 is heated to 24 °C. The outside temperature is assumed to be 5 °C for all simulations performed in this section. All assumptions and boundary conditions were kept similar to those used to calculate the results shown in Figure 2.4, with the exception of the air inlet temperature and airflow for all vents, which is shown in Table 2.3.

For case 1, as shown in Figure 2.5.a, room 3 does not reach 24 °C while the temperatures of the other rooms are increasing unpleasantly. Figures 2.5.b, 5c and 2.5.d show that the average HVAC system run-time over two rounds of heating and cooling would be 126, 75 and 75 s for cases 2, 3 and 4, respectively, to heat the rooms from 20 °C to 24 °C under an outside temperature of 5 °C. Moreover, it would take 408, 327 and 324 s for the rooms to cool from 24 °C to 20 °C for cases 2, 3 and 4, respectively.

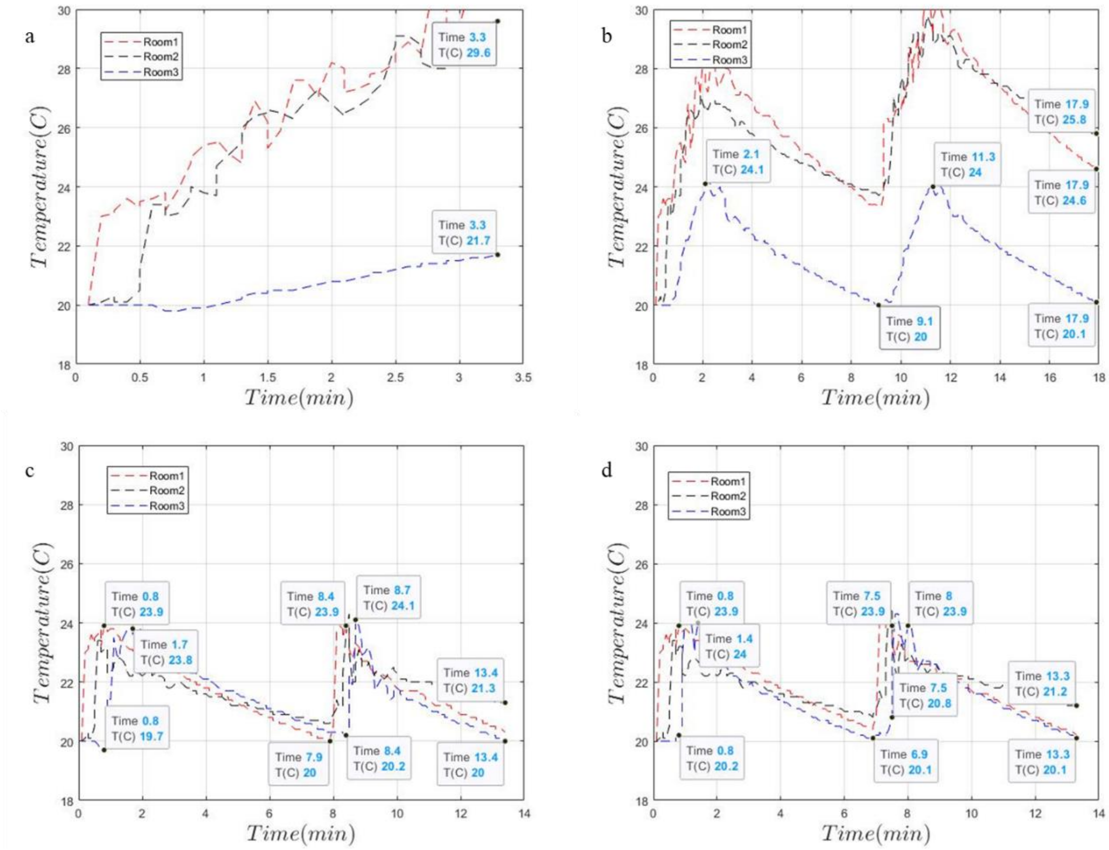

Figure 2.5. Simulation results for heating and cooling under an outside temperature of 5° (a) Without any fans or dampers (condition 1) (b) With a fan installed in one vent, but without any dampers (condition 2) (c) With dampers installed at the vents, but without any fans (condition 3) (d) With both fan and dampers installed (condition 4).

2.3.3 HVAC running hours

Based on the results shown in Figure 2.5, the number of hours the HVAC system is expected to run per day in order to maintain the desired temperature of 22 °C, assuming an outdoor temperature of 5 °C, are given in Table 2.4.

Table 2.4. HVAC run-time and down-time for cases 2, 3 and 4.

Outside temperature 5°C	Average run-time (s) for heating from 20 °C to 24 °C	Average down-time (s) for cooling from 24 °C to 20 °C	HVAC system run-time (h/day)
Case 2	126	408	5.6
Case 3	75	327	4.5
Case 4	75	324	4.5

Considering an outside temperature of 5 °C the HVAC system would be required to operate 5.6 hours every day to regulate the temperature of room 3 at 22 °C for condition 2, wherein a fan is installed at the fourth inlet, but no dampers are present. However, the temperature of the other rooms would increase unpleasantly. In comparison, the HVAC system is required to run 4.5 hours per day to keep the temperature of rooms at the desire level for condition 3 and 4, wherein dampers are installed in inlets 1, 2 and 3. For case 1, without any fans or dampers present, the HVAC run-time would be 24 h/day to maintain the room 3 temperature at the desire level, while the temperatures of the other rooms are excessively high.

Objective 1 of this thesis was to experimentally measure the effects of installing smart booster fans and dampers on the ability to regulate airflow and to numerically evaluate the extent to which these fans can reduce the duty cycle in HVAC systems. The results show that the smart booster fan can significantly improve, even by greater than a factor of two, the airflow to a vent at the end of a long duct-branch and also, the duty cycle of HVAC system can be reduced from 24 hr/day for the worst case scenario to 4.5 hr/day using smart booster fans and dampers which can operate based on the need and temperature of each room.

Chapter 3
Numerical investigation of heat transfer in air channels for thermal energy storage applications in buildings

3.1 Introduction

In this study the effects of the cross-sectional shape of air-channels on heat transfer from the internal surface of channels to air flowing through the channels is investigated.

Generally, different channel geometries and fin shapes are used in HVAC ducting systems or in systems that are used in conjunction with HVAC systems, such as TES systems. For example, the adsorption-based TES system discussed in Chapter One could be used to store thermal energy in HVAC systems. If an adsorption-based TES system were to be integrated in an HVAC system, the geometry of the ducts and fins would need to be designed to optimally exchange heat between the TES and HVAC systems. Different channel and bed shapes can be designed for these systems. Therefore, to find the optimum channel shape, heat transfer to air flowing through channels with common geometrical cross sections, such as circular, triangular, rectangular, and sinusoidal are considered in this chapter. Further, heat transfer to air flowing through beds comprising these air channel shapes are also investigated. The beds have a greater cross-sectional area than the channels and can be used in the design of ducts that transport larger volumes of air in HVAC systems. Numerical analyses are performed to investigate the outlet temperatures to optimize the shape of the air channels and beds. Results show the sinusoidal channel and bed have better performance in relation to the outlet temperature. Considering channels with a length of 100 mm, a surface area of 1770 m^2, and a wall-to-air heat transfer rate of 790 W/m^2, the air outlet temperature for the sinusoidal channel is about 57°C higher than that of the circular channel. Considering beds with a height of 5 mm and wall-to-air heat transfer rate of 790 W/m^2, the outlet temperature of the sinusoidal bed is about 10°C higher than the outlet temperature for a rectangular bed with similar surface area. The results are applicable to the design of TES units that could be used directly or indirectly (such as adsorbent beds for TES, wherein the adsorbent is in contact with or supplies heat to the walls of the air channels and beds) to supply heat to air passing through HVAC systems within buildings.

3.2 Materials and methods

3.2.1 Numerical analysis methods for determining heat transfer within channels

Numerical analyses was performed to compare the amount of heat transferred to air that passes through channels with different cross-sectional geometries. Four different cross-sectional geometries were considered: 1) circular, 2) triangular, 3) rectangular, and 4) sinusoidal. These channels are shown in Figure 3.1 and their dimensions are given in Table 3.1. The length, L, and internal surface area, A, for all channels is 100 mm, and 1770 mm^2, respectively. The characteristic parameter, a, and cross-sectional area for each channel differs as shown in Figure 6 and Table 5. All four channels have the same internal surface area of 1770 mm^2 which is assumed to provide a constant heat flux of 790 W/m^2. This value was selected for the heat flux because it yields reasonable outlet air temperatures. For each of the four channels, air enters the inlet with a velocity of 1 m/s, a temperature of 20 °C, and a constant density of 1.225 kg/m^3. For each channel, the outlet is assumed to have zero Pascal gauge pressure. Also, a no slip boundary condition has been applied at the contact surface between the air and the channels. CFD analysis was performed using Ansys software to determine the heat transferred to the air as it passes through the channels. The mesh properties used in the simulation for determining the heat transfer within channels are given in Table 3.2. Figure 3.2 shows the specified mesh for each case study. The number of elements for the sinusoidal channel is much higher than the other shapes because of its complexity in the shape and to have a solution that converges. Also, the dependency of the solution from the grid for all cases is studied. For instance, the number of elements used to simulate the sinusoidal channel is 298,240 and reducing this number by 40,690 causes a change in the results of only 3% (see Tables A1 and A2 and Figures A5 and A6 in the Appendix for details). The next step in carrying out the simulations is to choose the kind of solver, models, and solution methods. The pressure-based solver type is chosen. In this method, a pressure equation solves the restriction of continuity (also known as the mass conservation) of the velocity. Also, absolute velocity formulation is used to decrease the numerical diffusion and have a more precise solution. Since the objective of these simulations is to compare the shape of the channels, a steady state solver with no gravity is selected. To calculate the heat transfer equations, the energy model is selected. Considering the properties of air at 20°C such as density (1.2047 kg/m^3), dynamic viscosity (1.8205*10^{-5} kg/m.s) and also calculating the hydraulic diameters of the channels as 5.63 mm, 3.40 mm, 4.42 mm and 3.02 mm for the circular, triangular, rectangular and sinusoidal channel shapes, respectively, the Reynolds numbers for the circular, triangular, rectangular and sinusoidal channel shapes are 373, 225, 292 and 200, respectively, showing laminar flow for all channel shapes. In the solution methods, the least squares cell based is selected for the gradient, second order is selected for the pressure, and second order upwind method is used for the momentum and energy conservation equations. Thereafter, the hybrid initialization is used to initialize the boundary conditions and to set the initial temperature of the fluid at 20 °C. At the end 1000 iterations was selected for all simulations, however, for all cases the solutions converged before reaching the maximum number of iterations.

Table 3.1. Dimensions of the duct channels.

Shape	a (mm)	L (mm)	A (mm^2)	Cross-sectional area (mm^2)
Circular	5.63	100	1770	24.96
Triangular	5.90	100	1770	15.09
Rectangular	4.42	100	1770	19.58
Sinusoidal	5.00	100	1770	12.50

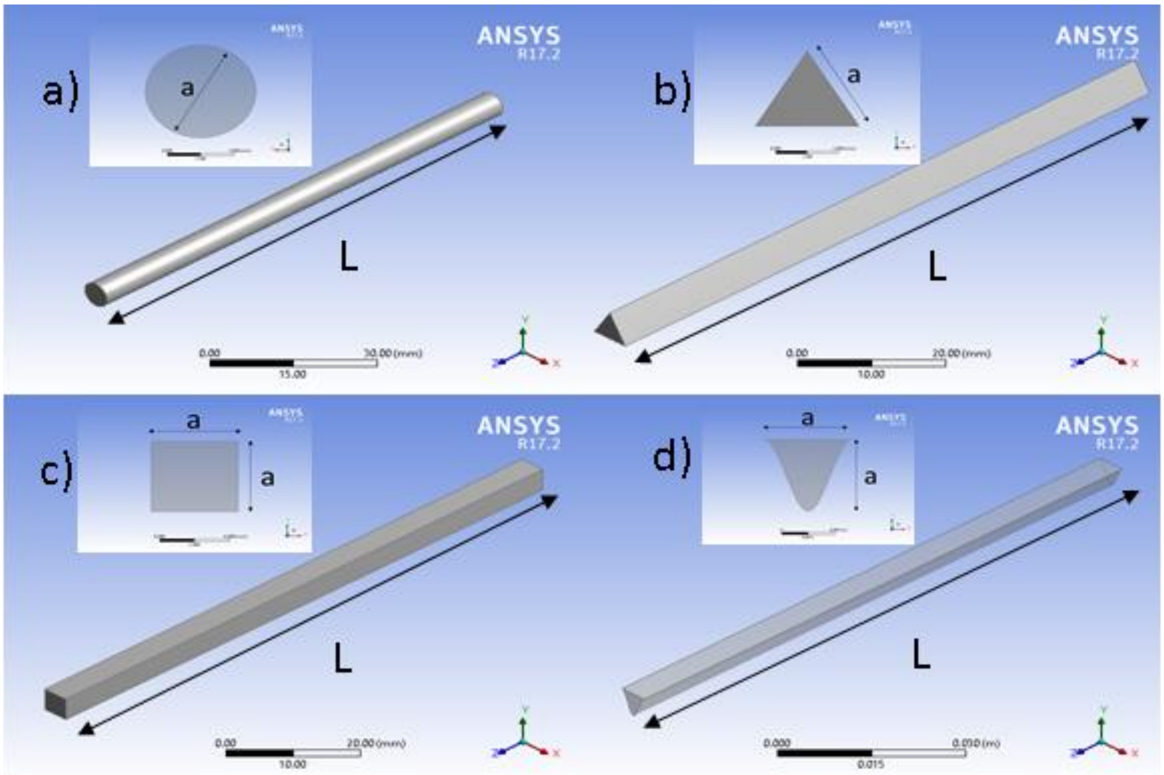

Figure 3.1. Geometry used in the simulation (a) Circular (b) Triangular (c) Rectangular (d) Sinusoidal.

Table 3.2. Mesh properties used in the simulations for the channels.

Shape	Min size (m)	Aspect ratio	Skewness	Growth rate	Number of elements
Circular	$1.46*10^{-5}$	1.64	0.240	1.2	4536
Triangular	$1.46*10^{-5}$	3.9	0.183	1.2	6768
Rectangular	$1.46*10^{-5}$	3.1	0.003	1.2	6390
Sinusoidal	$1.46*10^{-5}$	3.2	0.150	1.2	298240

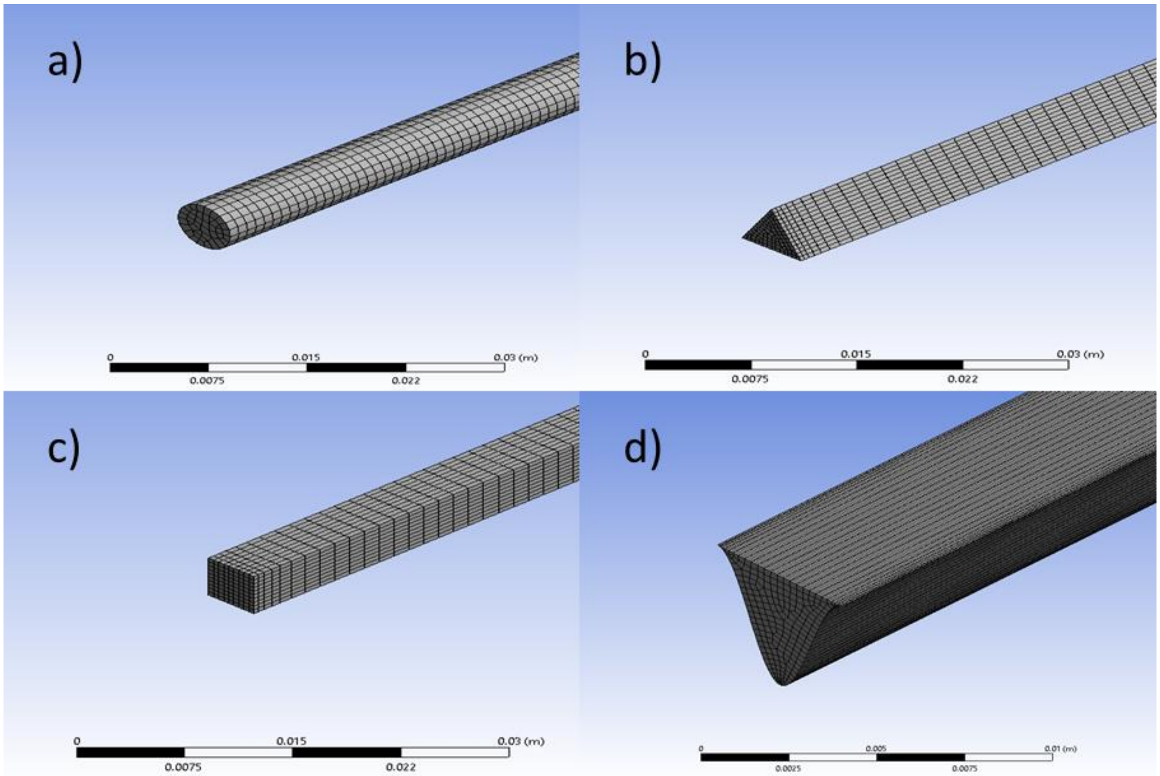

Figure 3.2. Specified mesh used in the simulation (a) Circular (b) Triangular (c) Rectangular (d) Sinusoidal.

3.2.2 Numerical analysis methods for determining heat transfer within beds

The heat transferred to air flowing through five bed designs with different shapes is numerically determined. The bed designs are based on five different shapes, which are: 1) Sinusoidal, 2) Triangular 1 (same width, d, and length, L, as the sinusoidal bed), 2) Triangular 2 (same internal surface area, A, as the sinusoidal bed), 3) Rectangular 1 (same width and length as the sinusoidal bed) and Rectangular 2 (same surface area as the sinusoidal bed). The geometry of the beds is shown in Figures 3.3 and 3.4 and the corresponding values for the dimensional parameters are given in Table 7. The height of all beds is assumed to have the same value of h = 5 mm. The internal surface of all beds is assumed to supply a constant heat flux of 790 W/m^2. The boundary conditions are similar to those used in simulating the channels. That is, air enters the inlet of the beds with a velocity of 1 m/s, a temperature of 20 °C, and a constant density of 1.225 kg/m^3. For each bed the outlet is assumed to have zero Pascal gauge pressure. Also, the outer side walls are assumed to be perfectly insulated. CFD analysis was performed using Ansys software to determine the heat transferred to the air as it passes through the beds. The mesh properties used in the simulation for determining the heat transfer within beds are given in Table 3.4. Figure 3.5 shows the specified mesh for each case study. The number of elements for the sinusoidal bed is much higher than the other shapes because this is needed to attain a solution that converges considering the increased complexity of its shape. Also, the dependency of the solution from the grid for all cases is studied. For instance, the number of elements used to simulate the sinusoidal duct is 575,865 and increasing this number by 130,071 causes a change in the results by only 1.5% (see Tables A3 and A4 and Figures A7 and A8 in the Appendix for details). The next step is to choose the kind of solver, models, and solution methods. The pressure-based solver type is chosen. In this method, a pressure equation solves the restriction of continuity (also known as the mass conservation) of the velocity. Also, absolute velocity formulation is used to decrease the numerical diffusion and have a more precise solution. Since the objective of these simulations is to compare the shape of the channels, a steady state solver with no gravity is selected. To calculate the heat transfer equations, the energy model is selected. Considering the properties of air at 20°C such as density (1.2047 kg/m^3), dynamic viscosity ($1.8205*10^{-5}$ kg/m·s) and also calculating the hydraulic diameters of the beds as 7.94 mm, 9.25 mm, 9.30 mm, 9.59 mm and 9.66 mm for the sinusoidal, triangular 1, triangular 2, rectangular 1 and rectangular 2 bed shapes, respectively, the Reynolds numbers for the sinusoidal, triangular 1, triangular 2, rectangular 1 and rectangular 2 bed shapes are 525, 612, 615 , 635 and 639, respectively showing laminar flow for all bed shapes. In the solution methods, the least squares cell based is selected for the gradient, second order is selected for the pressure, and second order upwind method is used for the momentum and energy conservation equations. Thereafter, the hybrid initialization is used to initialize the boundary conditions and to set the initial temperature of the fluid at 20 °C. At the end the 1000 number of iterations was selected for all simulations however, for all cases the solutions converged before reaching the maximum number of iterations.

Table 3.3. Dimension of beds.

Bed shape	H (mm)	D (mm)	L (mm)	A (mm^2)	Cross-section area (mm^2)
Sinusoidal	5	118	100	14341	590
Triangular 1	5	118	100	12064	590
Triangular 2	5	137.94	100	14341	689.7
Rectangular 1	5	118	100	11800	590
Rectangular 2	5	143.41	100	14341	717.05

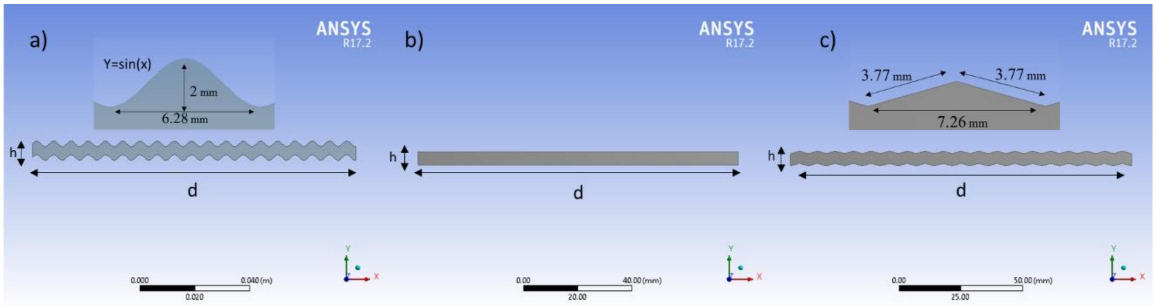

Figure 3.3. Cross-section schematic of modelled beds. (a) Sinusoidal (b) Rectangular (c) Triangular.

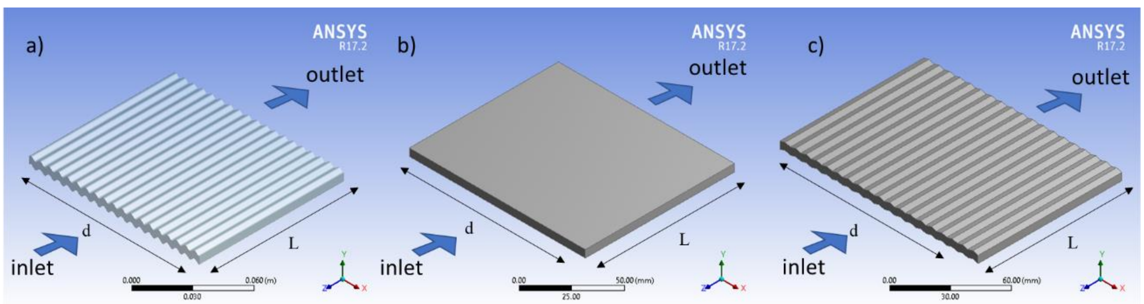

Figure 3.4. Geometry used in the simulation (a) Sinusoidal (b) Rectangular (c) Triangular.

Table 3.4. Mesh properties used in the simulations for the beds.

Shape	Min size (m)	Aspect ratio	Skewness	Growth rate	Number of elements
Sinusoidal	$1.46*10^{-5}$	1.68	0.342	1.2	575865
Triangular 1	$1.46*10^{-5}$	2.3	0.177	1.2	14740
Triangular 2	$1.46*10^{-5}$	2.5	0.180	1.2	15600
Rectangular1	$1.46*10^{-5}$	2.25	0.019	1.2	12420
Rectangular 2	$1.46*10^{-5}$	2.56	0.015	1.2	11890

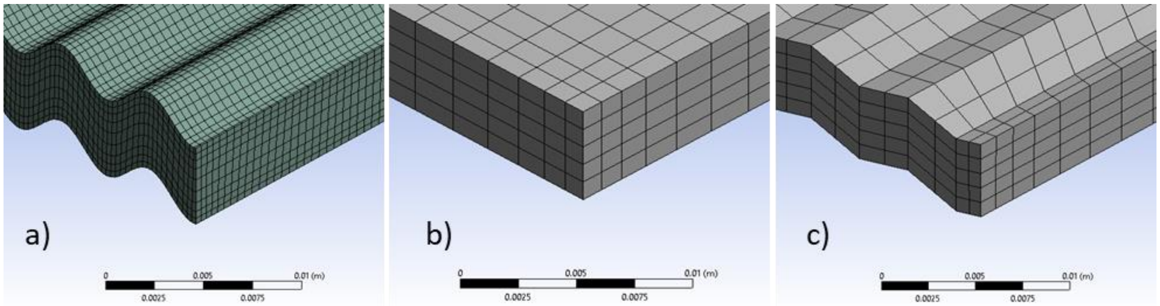

Figure 3.5. Specified mesh used in the simulation of the (a) Sinusoidal (b) Rectangular, and (c) Triangular beds.

3.3 Results

Figure 3.6 shows the average outlet temperature for the four different channel shapes studied. The results show that the sinusoidal shape has the highest outlet temperature of 136.3 °C. Accordingly, the average outlet temperatures for circular, triangular, and rectangular shapes are 79.3 °C, 122.9 °C, and 95.9 °C, respectively.

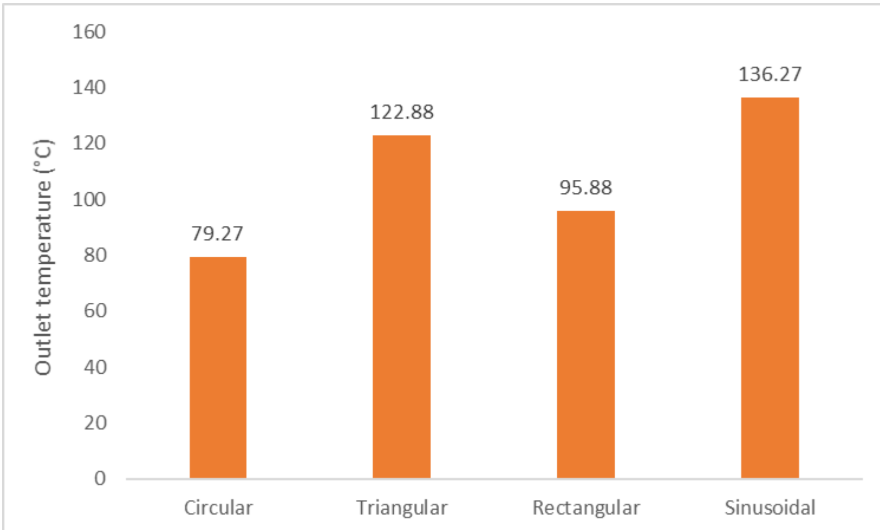

Figure 3.6. Average outlet temperature for different channel shapes.

Figure 3.7 shows the average outlet temperature for the five different bed shapes studied. The results show that the sinusoidal shaped bed has the highest outlet temperature of 65.9 °C. Accordingly, the average outlet temperatures for triangular 1 (same dimension as the sinusoidal), triangular 2 (same surface area as the sinusoidal), rectangular 1 (same dimension as the sinusoidal) and rectangular 2 (same surface area as the sinusoidal) are 58.3 °C, 58.2 °C, 56.3 °C and 56.3 °C, respectively.

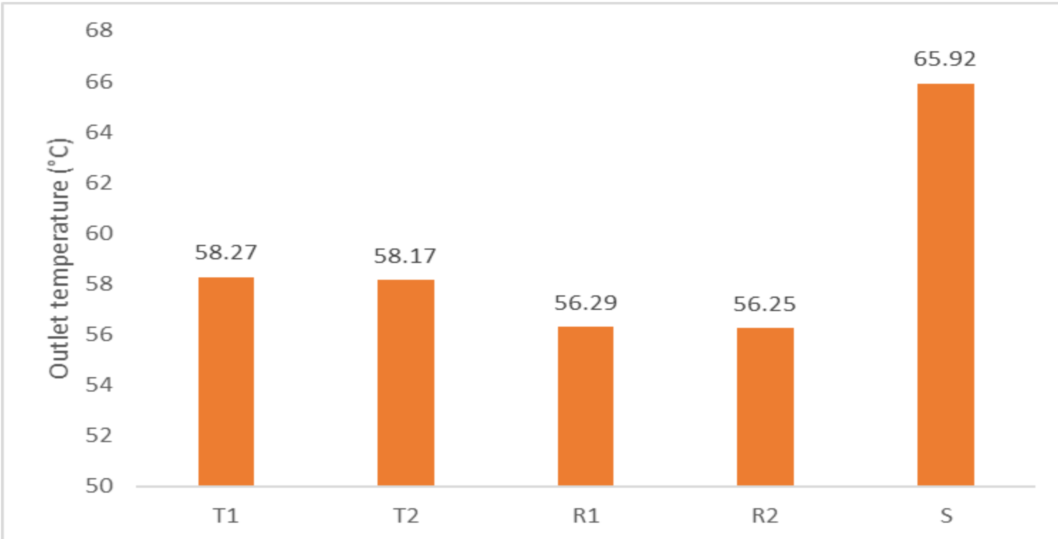

Figure 3.7. Average outlet temperature for triangular 1 (T1, same dimensions as the sinusoidal), triangular 2 (T2, same surface area as the sinusoidal), rectangular 1 (R1, same dimensions as the sinusoidal) and rectangular 2 (R2, same surface area as the sinusoidal).

Table 3.5. Inlet pressure of the channels.

Channels	inlet pressure (Pa)
Sinusoidal	7.71
Circular	2.29
Rectangular	3.27
Triangular	4.82

Table 3.6. Inlet pressure of the beds.

Beds	inlet pressure (Pa)
T1	1.19
T2	1.18
R1	1.13
R2	1.13
S	1.67

Table 3.5 and Table 3.6 show the inlet gauge pressure of the air for the channels and beds, respectively. Since the outlet pressures at the boundry conditions were set to zero-gauge pressure, the pressure drop for each case is equal to the inlet gauge pressures. It can be seen that for both channels and beds the sinusoidal shape results in a higher inlet pressure (7.71 Pa for the channel and 1.67 Pa for the bed) compared to all other cross-sectional shapes considered.

Tables 3.7 and 3.8 compare the wall-to-air heat transfer rate to the power loss due to the pressure drop along the channels and beds, respectively. It can be seen that the power lost for the sinusoidal channel and bed are higher than the other shapes.

Table 3.7. Power calculation of the channels from the heat transfer and drop pressure.

Channel shapes	Wall-to-air heat transfer (kJ/s)	Power loss due to pressure drop (kJ/s)
Circular	$1.82*10^{-3}$	$5.62*10^{-5}$
Triangular	$1.91*10^{-3}$	$7.15*10^{-5}$
Rectangular	$1.83*10^{-3}$	$6.30*10^{-5}$
Sinusoidal channel	$1.79*10^{-3}$	$9.48*10^{-5}$

Table 3.8. Power calculation of the beds from the heat transfer and drop pressure.

Bed shapes	Power gained from the heat transfer (kJ/s)	Power lost from the drop pressure (kJ/s)
Sinusoidal bed	$2.78*10^{-2}$	$9.69*10^{-4}$
Triangular 1	$2.78*10^{-2}$	$6.91*10^{-4}$
Triangular 2	$3.08*10^{-2}$	$8.00*10^{-4}$
Rectangular 1	$2.64*10^{-2}$	$6.56*10^{-4}$
Rectangular 2	$4.06*10^{-2}$	$7.97*10^{-4}$

3.4 Discussion

As shown in Figures 3.4 and 3.5 the temperature of the air flowing through the sinusoidal-shaped channels and beds increases to the greatest extent. These results can assist in the design of ducts with integrated TES. For example, phase change materials or adsorbent-based thermochemical energy storage materials may be applied at the surfaces of the ducts. Further, TES integrated into the ducting network of HVAC systems can potentially be coupled with HPs to efficiently utilize surplus electricity during low-demand periods. Future work is required to investigate the potential of such systems and the optimal duct design for their implementation.

Chapter 4
The Integration of adsorption-based thermal energy storage in HVAC systems

Adsorption-based TES units, when charged using renewable electricity and integrated into the ducts of building HVAC systems, offer a good pathway to help decarbonize buildings. In these units, hot air generated using clean electricity can be used to desorb an adsorbate from an adsorbent, thereby storing thermal energy. The thermal energy can be retrieved at a later time and used to heat air passing over the adsorbent, which can then be delivered indoors. These systems can be simple in design and do not need complicated instrumentation to operate. A range of adsorbents are available to meet indoor heating requirements. Further, the temperature of air entering the indoors can be controlled by controlling the airflow velocity of the air entering the TES system. In this work, an experimental set up is built wherein a TES unit is directly integrated into an HVAC duct branch. This TES unit uses silica-based materials to provide thermochemical energy storage. Hot air is used to “charge” the silica gel. The silica is left to cool to room temperature and thermal energy is subsequently retrieved by flowing humid air across the silica. Water in the humid air is adsorbed by the silica gel and the heat of adsorption is transferred to the air flowing past the silica gel. Experimental results are used to measure the amount and efficiency with which thermal energy is stored and the benefits of using “clean” excess electric power to charge the TES medium is evaluated.

4.1 Materials and methods

4.1.1 Experimental setup and measurements

An experimental set up is built wherein a TES unit is directly integrated into an HVAC duct branch. This TES unit uses silica-based materials to provide thermochemical energy storage. The experimental system contains several parts, which are listed below and labeled in Figure 4.1. The dimensions for the components in the experimental setup shown in Figure 4.1 are provided in Table 4.1.

1. Air blower heater and smart booster fan
2. Ducting system
3. Thermal energy storage bed
4. Sensors
5. Adsorbent material

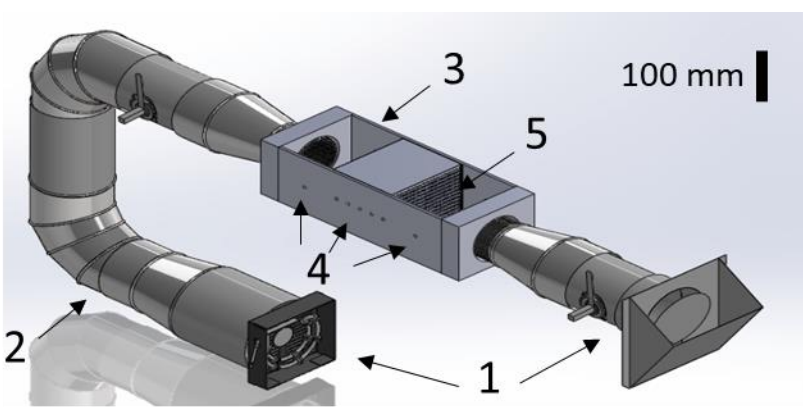

Figure 4.1. Schematic of the experimental system.

Air blower heater and smart booster fan:

An ipower Electric Heater, shown in Figure 4.2, with 1500 W power was used as a blower and also as a heater. It can heat the air up to 80°C. It is placed at the inlet of the experiment. A smart booster fan is also installed at the end of the ducting system to increase the airflow. The smart booster fan is a product from Smart Cocoon, Inc. with model number SC-SFV304X10.

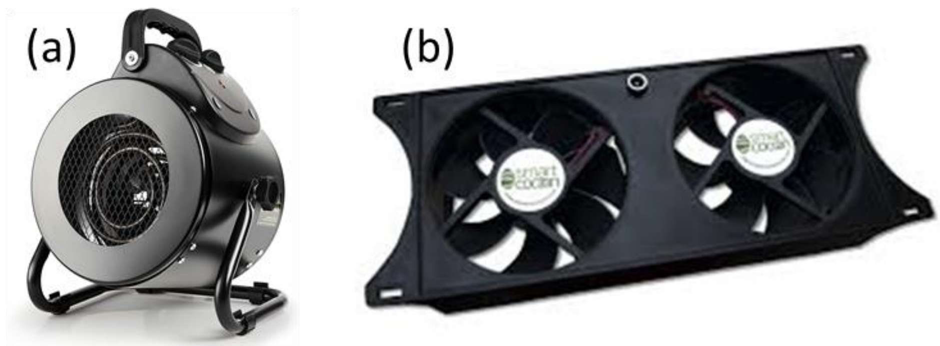

Figure 4.2. (a) iPower Electric Heater (b) Smart booster fan.

Ducting system

In the ducting system ducts with different sizes such as 8" and 4" were used. Reducers such as 8" to 6", 6" to 4", and 4" to 3" were also used. Two 4-inch Aluminum blast gates were used for opening, closing, and controlling the airflow of the system. Also, fiberglass insulation was used to insulate the ducting system. An air intake hood was installed at the end of the ducting system. The ducting system starts with an 8'' to 6'' duct reducer from the air blower heater and continues with a 6'' to 4'' duct reducer to connect with a 4'' duct. Due to the lack of experimental space in the lab a 180˚ bend was needed to install the TES bed at the top. Before and after the TES bed, two 4’’ to 3’’ duct reducers were used because of the 3’’ inlet and outlet of the bed. Also, two 4-inch aluminum blast gates were installed before and after the bed. Finally, a smart booster fan placed inside the air intake hood was installed at the end of ducting system.

Thermal energy storage bed

The TES bed contains two parts. The material container bed and the tank which are shown in Figure 4.3. The TES bed was 3D-printed using an ELEGOO UV Photocuring LCD 3D Printer which uses ELEGOO Photopolymer Resin as the material.

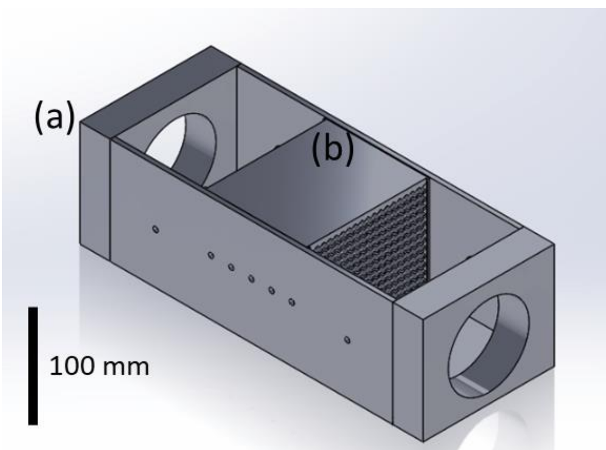

Figure 4.3. (a) The tank (b) The material container (of the thermal energy storage bed).

As discussed in Chapter Three, channels and beds with a sinusoidal cross section have better heat transfer performance in comparison to channels and beds with circular, triangular, or rectangular cross-sections. Therefore, in this study, the material container bed within the TES unitis designed to have sinusoidal fins inside it. Adsorbate beads (silica gel) were used in these experiments and the adsorbate remains in place when packed between the sinusoidal fins within the material container bed. Furthermore, there are five holes at the side of the material container bed for installing thermocouples which are described in the sensors section (Section 4.1.1.4). Table 4.1 represents the material container bed's properties. Figure 4.4 shows the material container bed.

Table 4.1. Properties of the material container bed

Dimension (mm) width * height* depth	120*100*104
Fin thickness (mm)	2
Number of fins	12
Diameter of the holes (mm)	5
Height between the fins (mm)	5

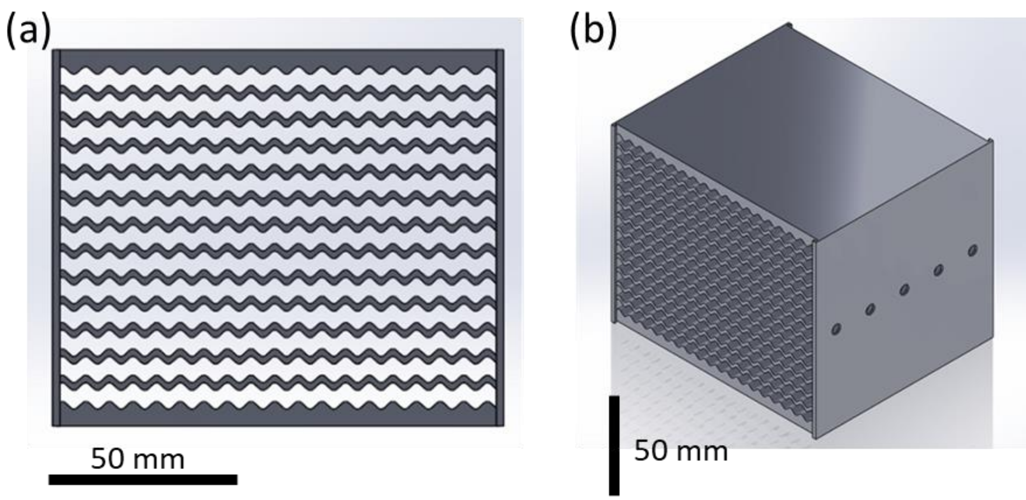

Figure 4.4. Schematic of the adsorption bed (a) Cross-sectional view of the sinusoidal fins, and (b) An isometric projection of the adsorption bed.

The tank that encloses the adsorption bed is designed in a way that the outer walls of the adsorption bed are in contact with the inner walls of the tank and the material container is placed inside it. This tank has an inlet and outlet, each with a 3” diameter. There are two holes for the humidity sensors at one side and seven holes for the thermocouples at the other side of the tank as shown in Figure 4.5. Table 4.2 presents the properties of the tank.

Table 4.2. Properties of the tank

Dimension (mm) length * height* depth	340*105*130
Diameter of the humidity sensor’s holes (mm)	16.2
Diameter of the thermocouples sensor’s holes (mm)	5
Diameter of the inlet and outlet hole (inch)	3
Thickness of the side walls (mm)	4.5

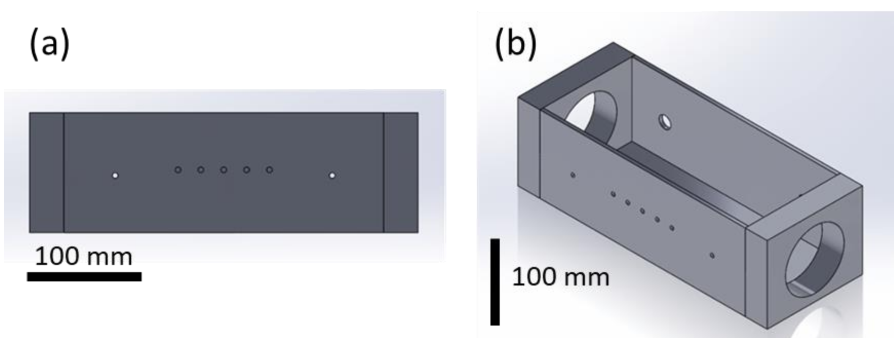

Figure 4.5. Schematic of the tank that holds the adsorption bed (a) Front view: the five holes for thermocouples that measure the temperature within the adsorption bed are at the middle of the tank and the white holes towards the end of the tank are for thermocouples that measure the inlet and outlet temperatures (b) Isometric view.

Figure 4.6 shows an image of the thermal storage bed used in the experiment which is made of photopolymer resin.

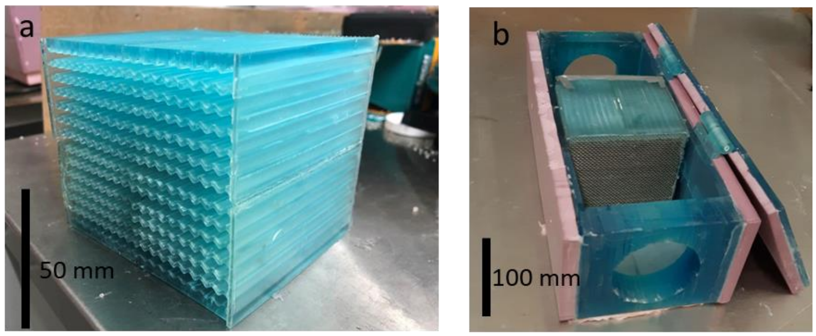

Figure 4.6. (a) The material container bed (b) The adsorption bed and tank.

Sensors

There are three kinds of sensors that are used in this experiment:

1) Thermocouples
2) Humidity sensors
3) Anemometer

Seven T-type thermocouples were used. They have been named T1 to T7 as shown in Figure 4.7 and Figure 4.8. T1 and T7 measure the inlet and outlet temperature of the air passing through the TES bed and T2 to T6 measure the temperature throughout the adsorption bed.

There are two humidity sensors installed in this experiment. RH_i and RH_o measure the relative humidity at the inlet and outlet of the TES bed.

An anemometer (Extech AN100) was used at the inlet of the TES bed to measure the velocity of the air flowing through the adsorption bed during the experiment.

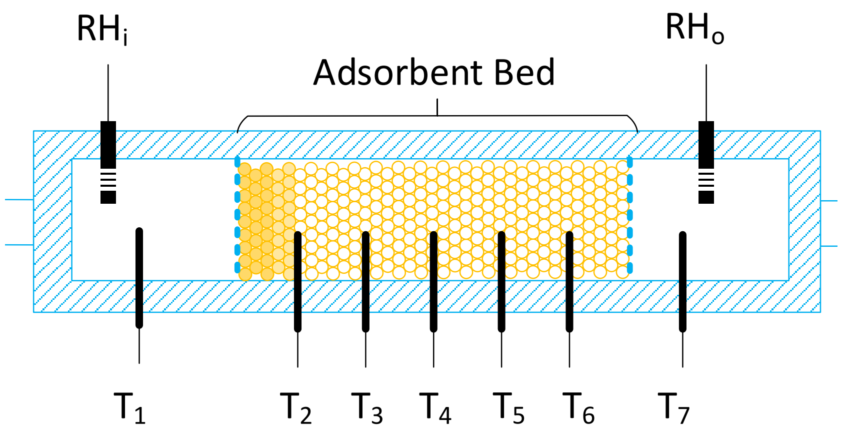

Figure 4.7. Schematic view of the thermocouples and humidity sensors.

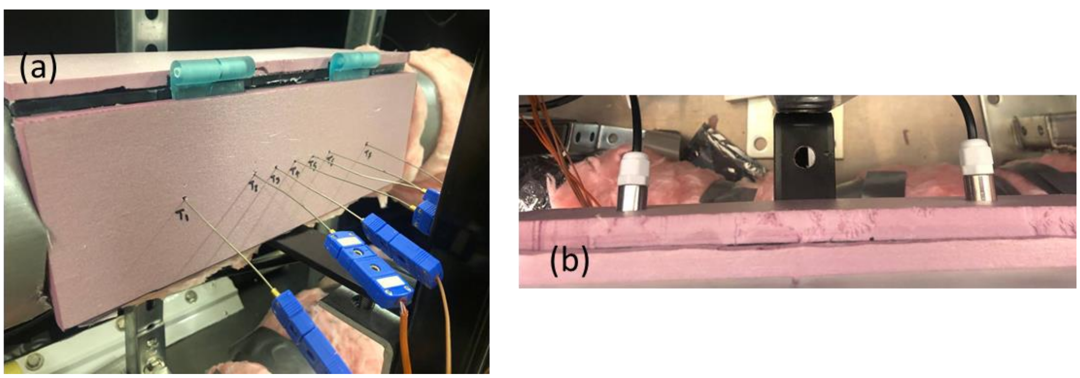

Figure 4.8. Experimental view of the (a) Thermocouples (b) Humidity sensors

The thermocouples and humidity sensors were connected to a LabJack T7-Pro data acquisition system. This data acquisition system uses Kipling software to be connected to the computer and LJLogM software to show the results in real time. The system was set to save the data every 10 seconds in a DAT file. Eventually, all the data was transferred to an excel file for further calculations.

Absorbent material

As explained in Chapter One, adsorption is an exothermic thermochemical surface process in which adsorbate particles adhere to the adsorbent surface. The adsorption process results in the decrease in the entropy of adsorbate molecules ($\Delta S < 0$), and the surface energy of adsorbent surface ($\Delta H < 0$) , which together gives it an exothermic character and causes adsorption heat. Adsorbents are highly porous materials having a high surface area and depending upon the pore diameter and polarization adsorb a variety of adsorbates.

In this experiment, orange silica gel is used as the adsorbent material. Silica gel is a type of silicon dioxide, having an amorphous structure of silicon and oxygen atoms with nanometer-sized pores. It has a high specific surface area of about 800 m^2/g. Silica gel is a safe, non-corrosive, cheap and abundant adsorbent. Table 4.3 shows the properties of the silica gel. The entropy of adsorbate molecules decreases when they are adsorbed on the adsorbent surface. The adsorption process results in a net surface energy decrease at the surface of the adsorbate material, which is giving it an exothermic character. The silica gel used in the experiment was attained from Dry & Dry company with product number CRH-16036. Orange silica gel changes color to dark green when it is saturated with moisture. Methyl violet within the silica gel changes in color due to changes in pH.

Table 4.3. Properties of the silica gel.

Silica gel	
Adsorption heat (kJ/kg)	2000-2500
Adsorbate	Water
Charging temperature (°C)	70-110
Energy density (kg/m^3)	650-700
Specific heat (kJ/kg·K)	0.8-0.9
Thermal conductivity (W/m·K)	0.15-0.20
Adsorbate uptake (g/g)	0.03-0.10

In total, 467 g of silica gel beads are placed inside the material container bed between the sinusoidal fins as shown in Figure 4.9. When cool humid air passes through the silica gel beads, the humidity is adsorbed by the silica gel and the heat of adsorption is released. On the other hand, when hot air passes over the silica gel beads, water is desorbed from their surface. The process in which cool air is heated as it passes through the beads and adsorption takes place is the discharging process, whereas the process in which desorption occurs as hot air passes though the material is the charging process.

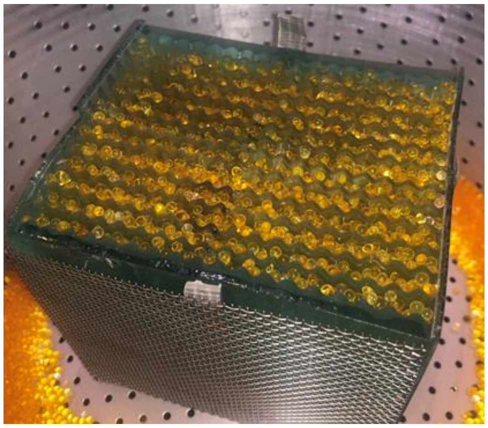

Figure 4.9. Silica gel beads inside the material container bed.

Eventually, after assembling the different parts of the experiment, Figure 4.10 shows the front view of the experimental set up in the lab.

Figure 4.10. Experimental setup, front view

4.1.2 Charging and discharging processes

This experiment includes two processes. The first is the “charging” process, wherein hot air passes through the adsorbent material (silica gel) which is saturated with the adsorbate (water). When hot air, at a temperature of ~80 °C, passes through the adsorbent material the adsorbate is desorbed and flows out of the adsorption bed. Ideally, after the charging process has been completed the adsorbent material will not have any adsorbate on its surface and is “fully charged”. However, in practice there is always some adsorbate molecules that remain on the surface of the adsorbent.

In the second process, called “discharging”, moist air passes through the adsorbent bed and across the surface of the silica gel, which is charged and ready to adsorb water from the humid air. As water is adsorbed by the silica gel the heat of adsorption is released, thereby heating the air flowing through the adsorption bed and hot air exits through the outlet.

4.2 Results

4.2.1 Charging process

Figure 4.11(a) shows the experimental results for the charging process. A blower is used to supply the hot air at a temperature of about 70 °C to charge the adsorbent materials. The blower uses a thermostat to switch a heater on and off to control the air temperature. Consequently, the temperature of the air entering the inlet of the adsorbent bed oscillates by about 5 °C, although the average inlet air temperature is ~70 °C. The hot air entering the TES bed interacts with the adsorbent (silica-gel) that is saturated with the adsorbate molecules (water) after previously being discharged. The adsorbate molecules are adsorbed on the adsorbent material surface with weak Vander Waal’s forces and need some energy to facilitate their desorption. Further, both adsorbent and adsorbate materials have some specific heat capacity. As is evident from Figure 4.11(a), the charging heat supplied by the blower, or the temperature of the heated air entering the TES bed is constant at about 70°C. However, the temperature inside the adsorbent material, which can be observed using thermocouples T2-T6, first rises with a steep slope, and then continues to rise at a lower rate for some time, after which the rate of temperature increase rises once again until the inlet air temperature of ~70 °C is reached. The initial rise in the temperature curves is largely because the heat from the incoming air is absorbed by the adsorbent and adsorbate materials in the form of sensible heat. Adsorbate molecules start desorbing from the adsorbent material surface once they have acquired enough thermal energy to reach the desorption energy which causes a rise in relative humidity at the outlet as shown in Figure 4.11(b). Further, the adsorbate molecules in the first zone, where thermocouple T2 is placed, desorb from the adsorbent material surface faster than the second zone, and so on till the last zone. For example, form the ~ 0.5 to 3 h point the experiment the temperature curve for T6 is the lowest and flattest, and T6 takes the longest to reach the temperature of the inlet air (~70 °C). The curve measured using T6 remains nearly flat over this time period because desorption is occurring this time; the temperature is almost constant as heat added to the adsorption bed is used to desorb water rather than providing sensible heat in the vicinity of T6. The rate of temperature increases from the ~ 0.5 to 3 h point of the experiment is progressively larger in moving from the end of the adsorption bed towards the beginning of the adsorption bed (e.g. over this time period the rate of temperature increase measured by T6 is less than that measured by T5, which is less than that measured by T4, and so on). The rate of temperature increases over the ~ 0.5 to 3 h point of the experiment is greater at points closer to the inlet of the adsorption bed because the desorption process begins at the inlet of the adsorption bed and gradually moves toward the outlet as hot air is continued to be supplied over the duration of the experiment. In other words, the temperature of T2 rises first followed by T3 and so on until T7 which indicates that the charging of the adsorption material happens in zones. Initial charging happens at the initial zone where T2 is placed, followed by the next zone where T3 is placed until the last zone where T6 is placed. As shown in Figure 4.11 (a) after about two hours of the charging process the temperature of the first zone inside the adsorption material (T2) reaches about 70 °C. About one hour later the second zone (T3) reaches 70 °C and after about six hours of the charging process all zones inside the adsorption bed (T2 to T6) reach ~70 °C, which is the lower end of the charging temperature range of the adsorption material (silica gel) as shown in Table 4.3. Once all adsorbate molecules are desorbed from the adsorbent material surface (e.g. the adsorbent material becomes charged) all the incoming heat sensibly heats the adsorbent material and its surroundings until all thermocouples in the adsorption bed have reached the incoming air temperature, which is evident from Figure 4.11 (a). However, as the relative humidity at the outlet did not reach the relative humidity at the inlet, even after 8 hours, the adsorbent materials were not completely charged. The results from the relative humidity measurements (Figure 4.11 (b)) show that the relative humidity at the inlet is about 10% and about 30% at the outlet. As it is shown in Figure 4.11(b), as the charging process begins the outlet RH (RH_o) is higher than the inlet RH (RH_i). This increase in RH is expected to occur as water desorbs from the silica gel during the charging phase.

The charging process lasted for 8 hours. As time passes over these 8 hours the outlet RH decreases because the adsorbate (water) available to desorb decreases as the charging process continues. The velocity of the air during this process was about 0.5 m/s. When the charging process was completed the blast gates at the inlet and outlet of the TES bed were closed completely so that no moist air can enter the TES bed. Also, the weight lost during the charging process is measured. The weight lost is the weight of the adsorbate (Water) that is vaporized and leaves the adsorption material. The weight loss in charging process is measured as 95 g. In this work, a time gap of 14 hours is maintained between the charging and discharging process.

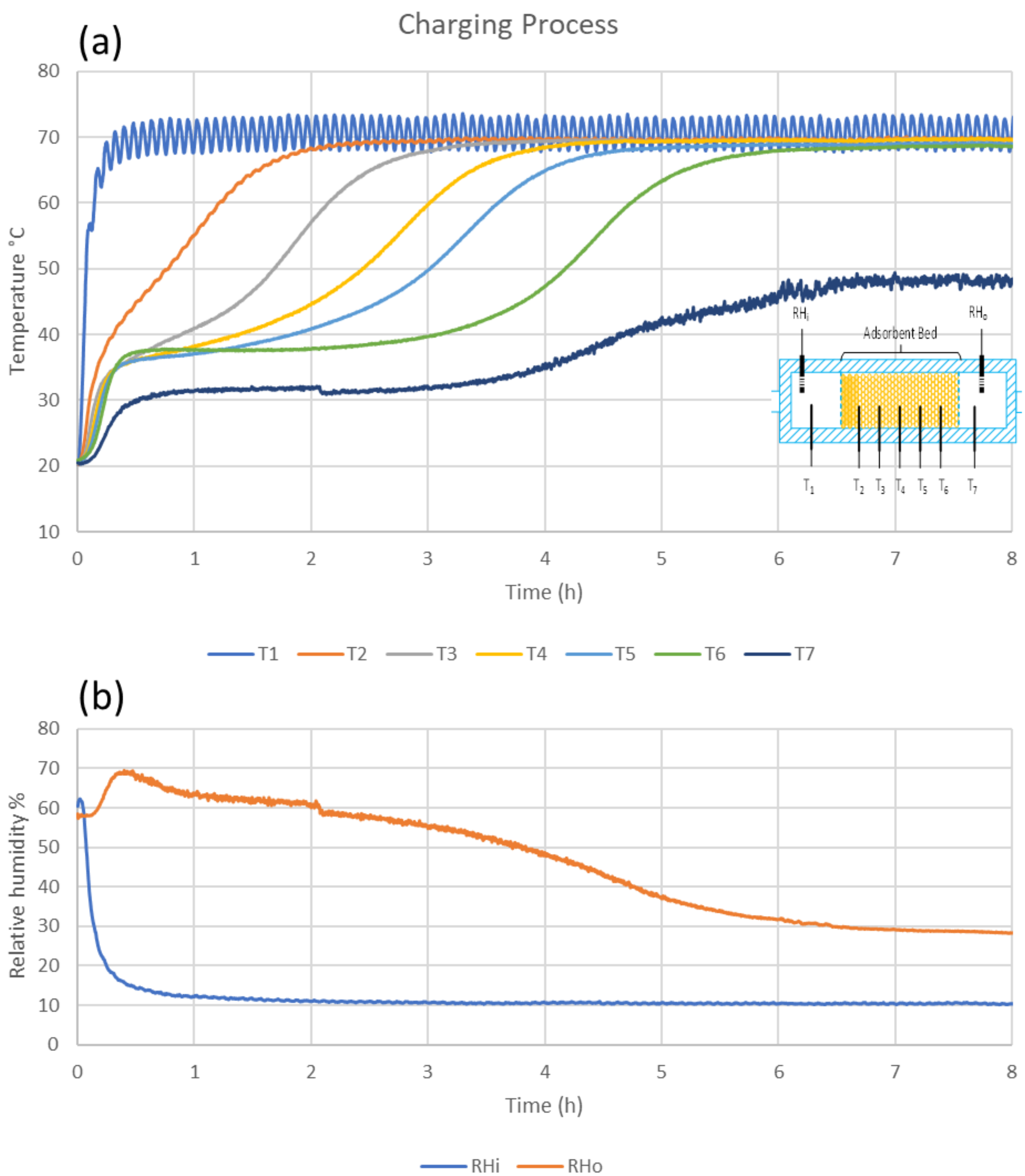

Figure 4.11. Experimental results for the charging process (a) Temperatures (b) Relative humidity.

4.2.1 Discharging process

During the discharging process water vapor present in the humid air entering the adsorption bed is adsorbed on the surface of the silica gel and the heat of adsorption is released. The heat of adsorption raises the temperatures of the adsorbent bed and the air flowing through it, which are measured using thermocouples.

Adsorption is a surface phenomenon with a limited number of active sites where adsorbate particles can be adsorbed. The adsorbent particles get completely discharged once all these active sites are filled with adsorbate particles. Therefore, inside the adsorption bed, adsorption takes places in a part wise manner. Initially, adsorption happens primarily in the adsorbent particles located next to the inlet. As the active sites near the inlet become covered with adsorbate particles, the active zone wherein most of the adsorption occurs, progressively shifts towards the outlet.

The process continues until all the active sites on the silica gel are covered with water, at which point the adsorbent is completely discharged. At this point the relative humidity at the outlet equals the relative humidity at the inlet.

To investigate the effects of airflow velocity, experiments were conducted to monitor the discharging process for three different inlet airflow velocities: 0.4 m/s, 0.6 m/s, and 0.8m/s. A total of nine experiments, three experiments with same airflow for each airflow rate, have been conducted. The weight gained in the discharging process is also measured for each airflow rate. The weight gained is the weight of the adsorbate adsorbed by the adsorbent material during the discharging process.

Figures 4.12, 4.13, and 4.14 show one example (out of three, other results are shown in the Appendix in Figures A9 to A14) of the temperature throughout the TES system and the relative humidity at the inlet and outlet of the adsorption bed when the air velocities into the adsorption bed were 0.4 m/s, 0.6 m/s, and 0.8 m/s over the duration of the discharging phase, which were ran for 20 hours, 10 hours, and 9.3 hours, respectively. The discharging phase is ran for a longer time as the air velocity decreases because the rate of adsorption increases when the air velocity is higher. A blower supplies the humid atmospheric air at 21.5 °C to facilitate the discharging process. This humid air enters the TES bed and interacts with the adsorbent material in the adsorption bed. Adsorption happens, the adsorbate (water) molecules present in the humid air form weak Vander Waal's bonds with the adsorbent material which results in the release of the heat of adsorption which is 2000-2500 kJ/kg when silica gel is used as the adsorbent material and water vapor as the adsorbate molecules, as is listed in Table 4.3. The heat of adsorption sensibly heats the adsorbent material and increases the outgoing air temperature, which can be observed using T7 and is plotted in Figure 4.12 (a), 4.13 (a), and 4.14 (a). A portion of the heat of adsorption is used to sensibly heat the reactor walls and some heat is lost to the surroundings.

During the discharging process adsorption initially takes place in the first zone where thermocouple T2 is placed followed by the second zone where T3 is placed and so on until the last zone where T6 is placed. As the adsorption takes place in the first zone, the heat of adsorption is released and increases in temperature at T2 until reaching the maximum temperature. At this point most of the adsorption material in the first zone is saturated, adsorption slows down, and the heat released due to adsorption decreases which causes a drop in the temperature at T2 until it reaches to a temperature equal to the incoming air temperature. In the meantime, adsorption peaks in second zone which causes the temperature at T3 to rise. This trend continues, as the temperature progressively peaks at locations further downstream in the adsorption bed and then gradually cools to the inlet air temperature, until the adsorption material is discharged. The highest temperature measured inside the TES bed is measured at T6. At the end of the experiment the adsorption bed was not completely discharged as the outlet relative humidity did not reach the level of the inlet relative humidity as shown in Figure 4.12 (b), 4.13 (b), 4.14 (b).

The weight gained during the charging process is measured to be 101.9 g, 103.7 g, and 103.2 g when the air flow rates were 0.4 m/s, 0.6 m/s, and 0.8 m/s, respectively. Table 4.4 shows the maximum temperatures and the time it took to reach the maximum temperature for T2, T3, T6, and T7.

Table 4.4. Maximum temperatures and the time taken to reach the maximum temperature during the discharging process for T2, T3, T6, and T7

	air flow rate: 0.4 m/s		**air flow rate: 0.6 m/s**		**air flow rate: 0.8 m/s**	
	Maximum temperature (°C)	Time (min)	Maximum temperature (°C)	Time (min)	Maximum temperature (°C)	Time (min)
T2	29.6	9	30	3.8	30	3.5
T3	36	22.5	35	8.5	34.5	7.5
T6	38.5	45	39	24	38	21
T7	28.3	80	28.4	34.5	27	27.5

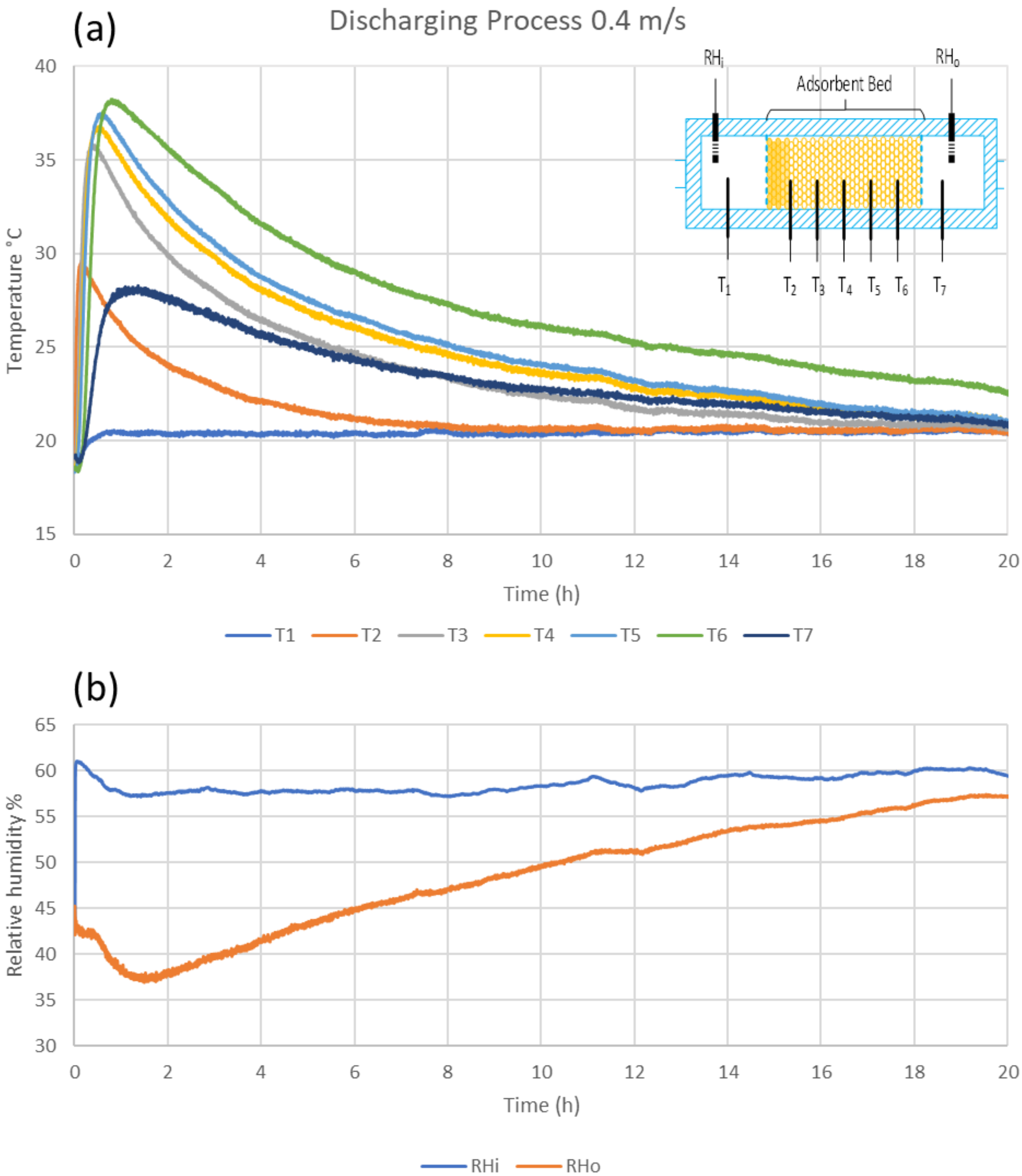

Figure 4.12. Experimental results for the discharging process at an air velocity of 0.4 m/s (a) Temperatures (b) Relative humidity.

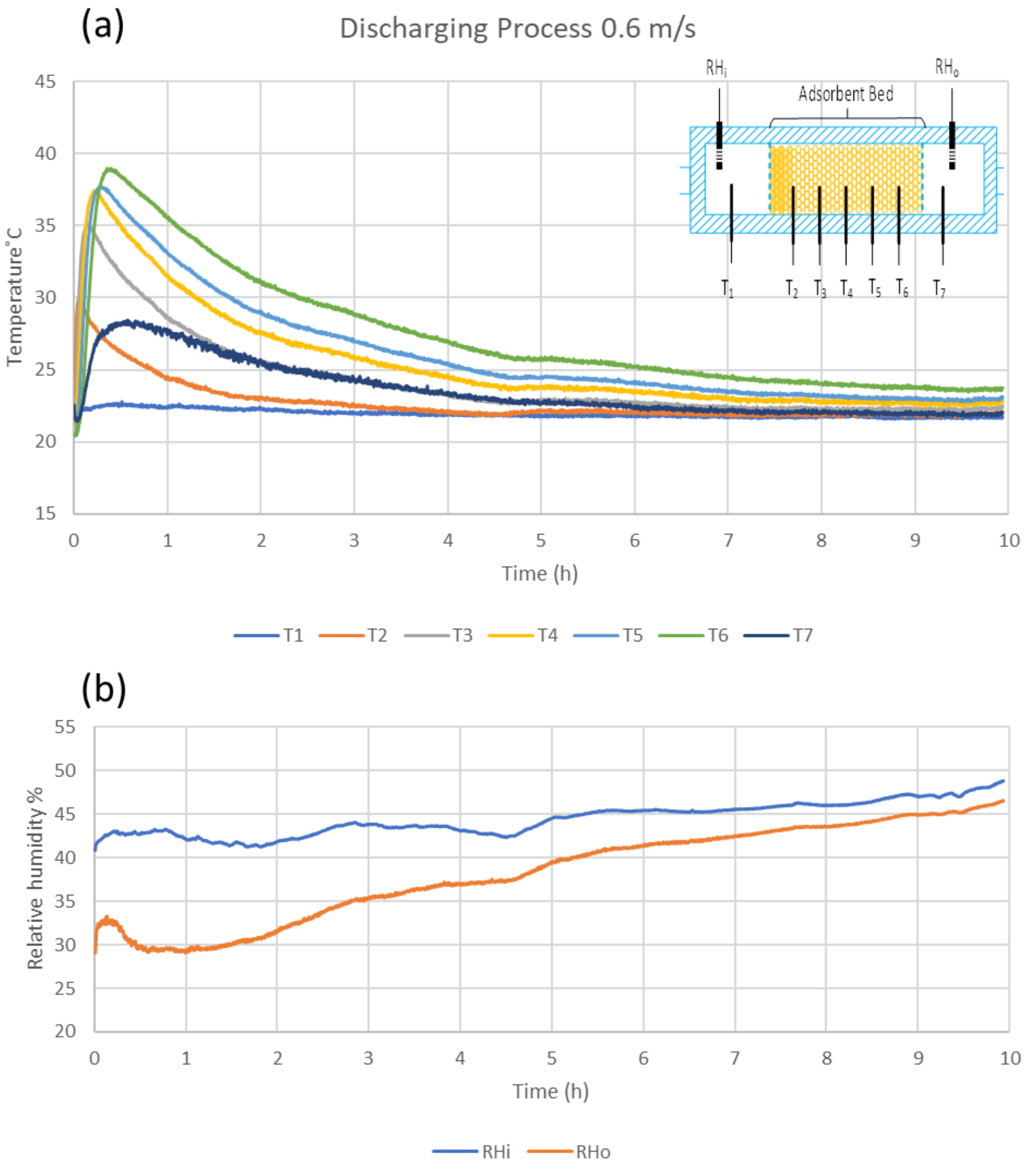

Figure 4.13. Experimental results for the discharging process at an air velocity of 0.6 m/s (a) Temperatures (b) Relative humidity.

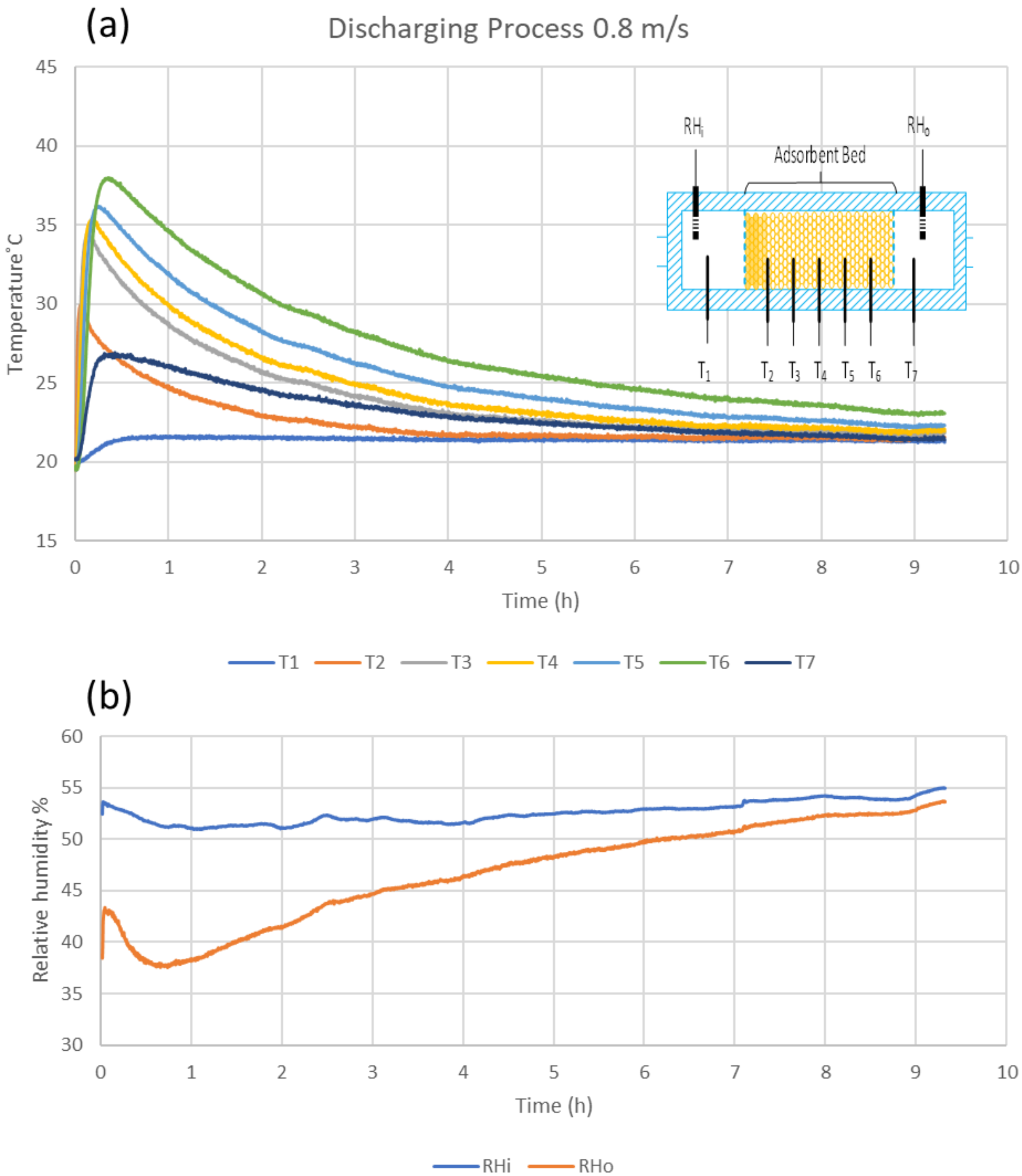

Figure 4.14. Experimental results for the discharging process at an air velocity of 0.8 m/s (a) Temperatures (b) Relative humidity.

4.2.2 Thermal energy storage efficiency

The focus of this study is to determine the energy extracted from the discharging process and the energy used for the charging process and to calculate the TES efficiency for the system. In order to do so, by using psychrometric calculations, the enthalpy at the inlet and outlet for each process has been calculated. By subtracting the enthalpies at the outlet from that at the inlet and multiplying the result into the mass of the air, the energy extracted from the discharging process and energy used for the charging process is calculated. Table 4.4 shows the energy used to heat the silica gel during the charging process and the energy retrieved during the discharging process. Considering that 467 g of silica gel is used in the experiment, the maximum amount of adsorption heat that could be released during the discharging phase is 934 kJ (Table 4.3). Also, the energy used during the charging process was calculated to be $7.8 * 10^3$ kJ. Herein, the energy extracted during the discharging processes divided by the maximum heat of adsorption that could be released by 467 g of silica gel is referred to as the storage capacity efficiency, η_{sc}. The TES efficiency, η_{tes}, is the total energy extracted from the adsorbent bed during the discharging processes divided by the total energy supplied to the bed during the charging process.

Table 4.5. Energy calculations

Process	Energy (kJ)	Storage capacity efficiency, η_{sc} Average (Best run)	TES efficiency, η_{tes} Average (Best run)	Duration (h)	Differential pressure (Pa)
Discharging speed 0.4 m/s	400	32 ± 6 % (42%)	3.7 ± 1.3 % (5%)	20	4
Discharging speed 0.6 m/s	420	36 ± 8 % (45%)	4 ± 1.3 % (5.3%)	10	5
Discharging speed 0.8 m/s	590	45 ± 12 % (63%)	5.4 ± 2.1 % (7.5%)	9.3	9

The storage capacity efficiency when the airflow rate during the discharge phase is 0.4 m/s, 0.6 m/s, and 0.8 m/s is 32 ± 6 %, 36 ± 8 %, and 45 ± 12 %, respectively, where the error on these values is determined using 80 % confidence levels and the result from three experiments with the same airflow for each airflow rate. The TES efficiency of the system for 0.4 m/s, 0.6 m/s, and 0.8 m/s is 3.7 ± 1.3 %, 4 ± 1.3 %, and 5.4 ± 2.1 %, respectively. The differential pressure between the inlet and outlet of the TES bed for 0.4 m/s, 0.6 m/s, and 0.8 m/s is measured as 4 Pa, 5 Pa, and 9 Pa, respectively. As the airflow increases, the thermal energy gained by the air during the discharging process increases. The main reason for this is due to conversion of enthalpy to thermal energy gained. By multiplying the enthalpy into the mass of air passing through the TES bed, which increases as the airflow of the air increases. Figure 4.15 shows that a temperature gain of more than 25 °C is recorded at T6 after 5 hours into the discharging process when the velocity is 0.4 m/s which is notably lower when the velocity is 0.6 m/s and 0.8 m/s. This signifies that the temperature of the outgoing air can be controlled by controlling the airflow velocity. Larger amount of heat can be delivered by a higher velocity but over a shorter period. On the other hand, a lower amount of heat can be delivered over a longer duration by using a low velocity. There seems to be a "penalty" or trade-off – when storing the heat for longer (slow and low heat delivery over a long period) the total amount of heat that is delivered is less than if the heat was delivered quickly. A Total of nine experiments, three experiments with same airflow for each airflow rate have been conducted and results not shown in this chapter are provided in Figures A9 – A14 in the Appendix. Figure 4.16 shows the average temperature change between outlet and inlet for the three airflow rate cases. The average maximum increase in air temperature (in going from the inlet to the outlet) at an 80% confidence level over three experimental runs for each airflow velocity of 0.4 m/s, 0.6 m/s, and 0.8 m/s was 7.5 ± 0.6 °C, 6.8 ± 1.4 °C, and 7.4 ± 0.9 °C, respectively. Moreover, the maximum temperature is reached sooner when the airflow velocity is 0.8 m/s as compared to when the airflow velocity is 0.6 m/s. Likewise, the maximum temperature occurs at a sooner time in the experiment when the airflow velocity is 0.6 m/s as compared to when the airflow velocity is 0.4 m/s.

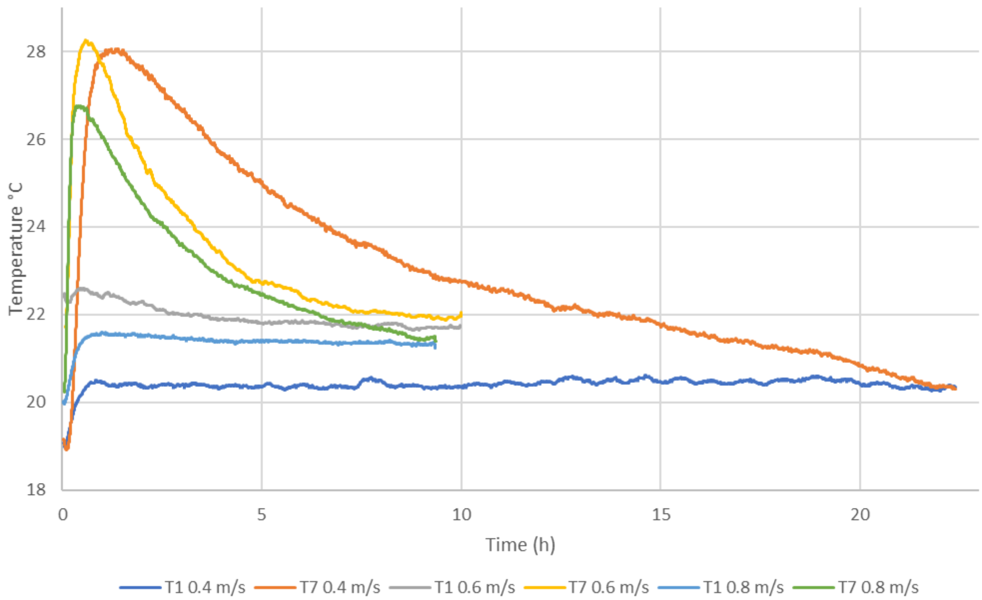

Figure 4.15. The inlet and outlet temperature for all three cases.

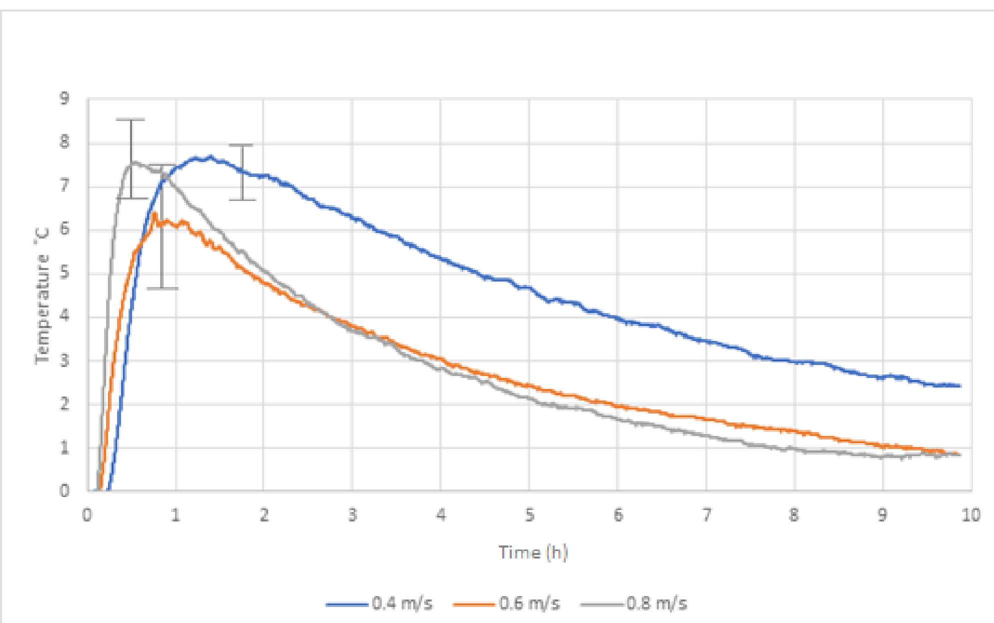

Figure 4.16. Average ΔT of inlets and outlets for all three cases.

As it is discussed in the background chapter, HPs can be coupled with this system for the charging process. It means that the heat provided by using electricity to power HPs can be used to charge this system and increase the TES efficiency. In order to show the effect of using HPs in the system, a study of a heat pump in a Canadian single-family house is considered. The COP of the HPs was calculated as 3.71 for the heating season [60]. If this HP is used for the charging process of the adsorption bed, the TES efficiency of the system for 0.4 m/s, 0.6 m/s, and 0.8 m/s, would increase to 19%, 19.9%, and 28%, respectively.

Furthermore, the TES efficiency can be improved by changing several factors such as optimizing the geometry of the TES bed, using different adsorbent materials, using more adsorbent material, and by increasing the inlet charging temperature.

The other advantage of this silica-based TES is that it is reusable after each charging and discharging process for a significant time. Also, unlike sensible and latent TES systems, the adsorption-based TES system described herein can store thermal energy indefinitely as long as it is sealed, and no adsorbate interacts with the adsorbent material.

Chapter 5
Conclusion

The focus of this thesis is to investigate the potential to enhance the performance of HVAC systems through the use of fans, dampers, and integrated TES. Low-powered fans placed in vents (booster fans) are investigated for their performance to improve heating and cooling and reduce HVAC system run times. Furthermore, "smart" booster fans and dampers are considered in the simulations by optimizing the times at which they can be turned on or off during the simulations. Duct systems with silica-based TES are also investigated. The silica-based TES system is charged using hot air, coming from a fan equipped with a resistive heater. Thus, the stored thermal energy is generated using electric power, providing an avenue for efficient electrification of heating in buildings.

5.1 Conclusion for evaluation of smart booster fans and dampers for advanced HVAC systems (Chapter two)

In this research, the ability of smart booster fans and dampers to regulate airflow in a long duct-branch has been investigated. The poor airflow to the last inlet in the duct-branch is due to friction caused by the length, curvature, and other inlets. It should be noted that the case wherein poor airflow is caused by a damaged or leaking duct work is not investigated in this case. Furthermore, regulations pertaining to air ventilation rates and use of dampers in HVAC duct work was not considered.

Airflow measurements on a prototype ducting system were performed to evaluate the ability of a smart booster fan to improve HVAC system performance in residential homes. Results show that the smart booster fan can significantly improve, even by greater than a factor of two, the airflow to a vent at the end of a long duct-branch. These results were also used in the designing of the TES bed and ducting system in chapter four. Numerical analysis shows that rooms in residential homes that suffer from poor airflow may never reach comfortable conditions during typical winter conditions. However, under typical conditions this problem can be fixed by installing a smart booster fan in this room.

Based on the results attained thus far and those reported herein, it does not appear to be beneficial to simultaneously operate multiple smart booster fans in the same duct branch, although results would vary on a case by case basis. Also, results from simulations show that smart dampers have potential towards enhancing temperature regulation while decreasing the duty cycle of HVAC systems. Table 2.4 showed that the duty cycle of HVAC system can be reduced from ideally 24 hr/day to 4.5 hr/day using smart booster fans and dampers which can operate based on the need and temperature of each room.

5.2 Conclusion for numerical investigation of heat transfer in air channels for thermal energy storage applications in buildings (Chapter three)

This research demonstrates a study on determining the heat transfer within differently shaped duct channels and beds using numerical analysis (CFD) and compares the outlet temperatures for four cases studied. Circular, triangular, square, and sinusoidal duct shapes are considered.

In a heating application, wherein heat is transferred from the internal surfaces of the ducts to the air, the sinusoidal channel and bed increased the temperature of the air more than the other cross-sectional shapes considered. For a set heating rate and surface area, the outlet temperature of the sinusoidal channel is about 57 °C higher than the circular channel, whereas the outlet temperature of the sinusoidal bed is about 10 °C higher than that of a rectangular bed. Energy losses due to the pressure drop in the channels and beds with a sinusoidal-shaped cross-section are greater than those in channels and beds with triangular or rectangular cross-sections. However, the energy losses due to pressure drop are small in comparison to the heat gained from the internal surfaces of the channels and beds for the conditions considered in this work (a wall-to-air heat transfer rate of 790 m/s). Thus, for the conditions considered in this work, the sinusoidal cross-sectional shape shows better performance than the triangular, rectangular, or circular cross-sectional shapes for both channels and beds. The results obtained from Chapter Three were considered when designing the optimum TES bed in Chapter Four. Sinusoidal beds can assist in the design of the TES bed by applying the adsorbate material on the surface of sinusoidal fins.

5.3 Conclusion for the Integration of adsorption-based thermal energy storage in HVAC systems (Chapter four)

An experimental set up is built wherein a TES unit is directly integrated into an HVAC duct branch. This TES unit uses silica-based materials to provide thermochemical energy storage. Hot air is used to charge the silica gel. The silica gel is left to cool to room temperature and thermal energy is subsequently retrieved by flowing humid air across the silica. Experimental results are used to measure the amount and COP with which thermal energy is stored and the benefits of using clean excess electric power to charge the TES medium is evaluated.

The results from the experiment show that a small amount of thermal energy (e.g., about 7.5%) can be stored using the silica-based TES unit. While this result is low, it is still a very good result considering this is the first study of its kind. Furthermore, it is recognized that the overall electric power-to-thermal energy conversion efficiency of the process can be greatly improved (e.g., from 5% to about 26%) by using a HP and taking advantage of its COP (assumed to be ~3.7 in this work) in conjunction with the TES unit.

5.4 Future works

Further work should be done to validate the numerical results attained in Chapter Two. However, this may require installing smart booster fans and dampers in the HVAC system inside a large-scale model or an actual building. Experiments should also be performed to validate the results from Chapter Three by fabricating circular, triangular, square and sinusoidal ducts and carrying out airflow and pressure measurements. Also, the performance of the TES system studied in Chapter Four can be improved to reach the desired outlet temperature (about 40 °C) by changing several factors such as optimizing the geometry of the TES bed, using different adsorbent materials, using more adsorbent material, and increasing the inlet charging temperature. Moreover, there is room to optimize how the adsorbent is loaded onto the fins within the TES bed. For example, future designs could consider applying the adsorbent to the surface of the fins within the test bed, leaving more space for airflow. These improvements will further the development of HVAC-integrated

TES systems that can be used for the electrification of heating. This is particularly useful in regions that have a low-carbon electric power system and surplus electricity, which can then be used for heating instead of fossil fuels.

References

[1]. International Energy Agency, Energy Efficiency Indicators Highlights Int. Energy Agency, 2017.

[2]. Residential Sector - Energy Use Analysis, Natural Resources Canada, oee.nrcan.gc.ca, 2016, accessed on February 11, 2020, http://bit.ly/2HfKso4.

[3]. Cuddihy J, Kennedy C, Byer P. Energy use in Canada: environmental impacts and opportunities in relationship to infrastructure systems. Canadian Journal of Civil Engineering. 2005 Feb 1;32(1):1-5.

[4]. Total End-Use Sector – GHG Emissions, Natural Resources Canada, oee.nrcan.gc.ca, 2016, accessed on February 11, 2020, <http://bit.ly/2UG4L5T>.

[5]. Ghajarkhosravi M, Huang Y, Fung AS, Kumar R, Straka V. Energy benchmarking analysis of multi-unit residential buildings (MURBs) in Toronto, Canada. Journal of Building Engineering. 2020 Jan 1;27:100981.

[6]. Balvers J, Bogers R, Jongeneel R, van Kamp I, Boerstra A, van Dijken F. Mechanical ventilation in recently built Dutch homes: technical shortcomings, possibilities for improvement, perceived indoor environment and health effects. Architectural Science Review. 2012 Feb 1;55(1):4-14.

[7]. Goetzler W, Guernsey M, Young J. Research & development roadmap for emerging HVAC technologies. Department of Energy, 2014 Oct.

[8]. Chenari B, Carrilho JD, da Silva MG. Towards sustainable, energy-efficient and healthy ventilation strategies in buildings: A review. Renewable and Sustainable Energy Reviews. 2016 Jun;1(59)1426-47.

[9]. Lin Z, Lee CK, Fong KF, Chow TT. Comparison of annual energy performances with different ventilation methods for temperature and humidity control. Energy and Buildings. 2011 Dec 1;43(12):3599-608.

[10]. Clements-Croome DJ, Awbi HB, Bakó-Biró Z, Kochhar N, Williams M. Ventilation rates in schools. Building and Environment. 2008 Mar 1;43(3):362-7.

[11]. Seppanen OA, Fisk WJ. Summary of human responses to ventilation. Indoor air. 2004, 14: 102-118.

[12]. Jahantigh N, Keshavarz A, Mirzaee M Optimization of hybrid heating system of residential buildings in different climates of Iran to provide thermal comfort. Mech Struct Fluids. 2013;3:97–108.

[13]. Delavari A, Ghassabi G, Saffarian MR. Numerical and experimental investigation of the effect of air conditioning duct on the room temperature distribution and energy efficiency. Journal of the Brazilian Society of Mechanical Sciences and Engineering. 2020 Jan;42(1):1-8.

[14]. Fisk WJ, De Almeida AT. Sensor-based demand-controlled ventilation: a review. Energy and buildings. 1998 Dec 1;29(1):35-45.

[15]. Nassif N. A robust CO_2-based demand-controlled ventilation control strategy for multi-zone HVAC systems. Energy and buildings. 2012 Feb 1;45:72-81.

[16]. Wang J, Tse NC, Poon TY, Chan JY. A practical multi-sensor cooling demand estimation approach based on visual, indoor and outdoor information sensing. Sensors. 2018 Nov;18(11):3591.

[17]. Huang H, Chen L, Mohammadzaheri M, Hu E. A new zone temperature predictive modeling for energy saving in buildings. Procedia Engineering. 2012 Jan 1;49:142-51.

[18]. Cao X, Dai X, Liu J. Building energy-consumption status worldwide and the state-of-the-art technologies for zero-energy buildings during the past decade. Energy and buildings. 2016 Sep 15;128:198-213.

[19]. Environmental Commissioner of Ontario, Making Connections Straight Talk About Electricity in Ontario, 2018, Energy Conservation Progress Report, Volume One (2018) at 94-109, online (pdf): Office of the Auditor General of Ontario, accessed on April 25, 2018, <www.auditor.on.ca/en/content/reporttopics/envreports/env18/MakingConnections>.

[20]. US Energy Information Administration. Annual energy outlook, 2014, accessed on December 16, 2014, <https://www.eia.gov/outlooks/aeo/>.

[21]. Martinopoulos G, Papakostas KT, Papadopoulos AM. A comparative review of heating systems in EU countries, based on efficiency and fuel cost. Renewable and Sustainable Energy Reviews. 2018 Jul 1;90:687-99.

[22]. Matthews H, Hendrickson C, Matthews D. Life cycle assessment: quantitative approaches for decisions that matter. Open access textbook, Retrieved (2014) Feb 3, 2021, <https://www.lcatextbook.com/>.

[23]. Winther BN, Hestnes AG. Solar versus green: the analysis of a Norwegian row house. Solar energy. 1999 Sep 1;66(6):387-93.

[24]. Adalberth K, Energy use and environmental impact of new residential buildings, Ph.D. Thesis, Department of Building Physics, Lund Institute of Technology, Lund, 2000.

[25]. Scheuer C, Keoleian GA, Reppe P. Life cycle energy and environmental performance of a new university building: modeling challenges and design implications. Energy and buildings. 2003 Nov 1;35(10):1049-64.

[26]. Abdulateef A, Mat S, Abdulateef J, Sopian K, Al-Abidi AA. Geometric and design parameters of fins employed for enhancing thermal energy storage systems: a review. Renewable and Sustainable Energy Reviews. 2018 Feb 1; 82:1620-35.

[27]. Eslami M, Bahrami MA. Sensible and latent thermal energy storage with constructal fins. International journal of hydrogen energy. 2017 Jul 13;42(28):17681-91.

[28]. Diao YH, Liang L, Zhao YH, Wang ZY, Bai FW. Numerical investigation of the thermal performance enhancement of latent heat thermal energy storage using longitudinal rectangular fins and flat micro-heat pipe arrays. Applied Energy. 2019 Jan 1;233:894-905.

[29]. Mohan A, Praveen A, Prasanthkumar P. Validation of HVAC System Design using CFD Modelling, 2016 December 5; 49:10079-83.

[30]. Shah V, Patil M. duct designing in air conditioning system and its impact on system performance, International Research Journal of Engineering and Technology (IRJET), 2019 July, Volume: 06 Issue: 07.

[31]. Rezanejadzanjani B, O'Brien P, Evaluation of Smart Booster Fans and Dampers for Advanced HVAC Systems, Journal of Green Building, 2021;16(2):115-27.

[32]. Kundu P, Cohen I, Hu G, Dowling D. Fluid mechanics 6th ed., waltham, ma.

[33]. Batchelor G. An Introduction to Fluid Dynamics. Cambridge Univ.Press. Cambridge, England. 1967.

[34]. Launder B, and Spalding D. Lectures in Mathematical Models of Turbulence. Academic Press, London, England. 1972.

[35]. Yakhot V, Orszag SA. Renormalization group analysis of turbulence. I. Basic theory. Journal of scientific computing. 1986 Mar;1(1):3-51.

[36]. Shih TH, Liou WW, Shabbir A, Yang Z, Zhu J. A new k-ϵ eddy viscosity model for high Reynolds number turbulent flows. Computers & fluids. 1995 Mar 1;24(3):227-38.

[37]. Bataille C, Sawyer D, Melton N. Pathways to deep decarbonization in Canada. Sustainable Development Solutions Network; 2015.

[38]. Steinberg D, Bielen D, Eichman J, Eurek K, Logan J, Mai T, McMillan C, Parker A, Vimmerstedt L, Wilson E. Electrification and decarbonization: exploring US energy use and greenhouse gas emissions in scenarios with widespread electrification and power sector decarbonization. National Renewable Energy Lab. (NREL), Golden, CO (United States); 2017 Jul 19.

[39]. Shipley J, Lazar J, Farnsworth D, Kadoch C. Beneficial electrification of space heating. Regulatory Assistance Project (RAP); 2018 Nov.

[40]. US Department of Energy, Office of Energy Efficiency & Renewable Energy. Heat pump systems. Accessed on September 25, 2005, <https://www.energy.gov/energysaver/heat-and-cool/heat-pump-systems>.

[41]. Arteconi A, Hewitt NJ, Polonara F. Domestic demand-side management (DSM): Role of heat pumps and thermal energy storage (TES) systems. Applied thermal engineering. 2013 Mar 1;51(1-2):155-65.

[42]. Karim MA. Experimental investigation of a stratified chilled-water thermal storage system. Applied Thermal Engineering. 2011 Aug 1;31(11-12):1853-60.

[43]. Li ZF, Sumathy K. Performance study of a partitioned thermally stratified storage tank in a solar powered absorption air conditioning system. Applied Thermal Engineering. 2002 Aug 1;22(11):1207-16.

[44]. Han YM, Wang RZ, Dai YJ. Thermal stratification within the water tank. Renewable and Sustainable Energy Reviews. 2009 Jun 1;13(5):1014-26.

[45]. Sarbu I, Sebarchievici C. A comprehensive review of thermal energy storage. Sustainability. 2018 Jan;10(1):191.

[46]. Patteeuw D, Bruninx K, Arteconi A, Delarue E, D'haeseleer W, Helsen L. Integrated modeling of active demand response with electric heating systems coupled to thermal energy storage systems. Applied Energy. 2015 Aug 1; 151:306-19.

[47]. Sarbu I, Sebarchievici C. Solar heating and cooling systems: Fundamentals, experiments and applications. Academic Press; 2016 Oct 18

[48]. Beckmann G, Gilli PV. Thermal energy storage: Basics, design, applications to power generation and heat supply.

[49]. Bauer T et. al, Thermal energy storage materials and systems, Annual review of heat transfer, ISSN: 2375-0294, Vol. 15, pages 131-177.

[50]. Dincer I, Rosen MA. Thermal energy storage: Systems and applications. John Wiley & Sons; 2011 Jun 24.

[51]. Gabelman A. Adsorption basics: part 1. Chemical Engineering Progress. 2017;113(7):48-53.

[52]. Seader JD, Henley EJ, Roper DK. Separation process principles. Chemical and biochemical operations, John Wiley & Sons. Inc., New Jersey. 2011.

[53]. Bonner OD, Smith LL. A selectivity scale for some divalent cations on Dowex 50. The Journal of Physical Chemistry. 1957 Mar;61(3):326-9.

[54]. Kubota M, Ueda T, Fujisawa R, Kobayashi J, Watanabe F, Kobayashi N, Hasatani M. Cooling output performance of a prototype adsorption heat pump with fin-type silica gel tube module. Applied Thermal Engineering. 2008 Feb 1;28(2-3):87-93.

[55]. Aristov Y, Glaznev I, Girnik I. Optimization of adsorption dynamics in adsorptive chillers: loose grains configuration. Energy. 2012 Oct 1;46(1):484-92.

[56]. Wang D, Zhang J. Design and performance prediction of an adsorption heat pump with multi-cooling tubes. Energy Conversion and Management. 2009 May 1;50(5):1157-62.

[57]. Zhang LZ, Niu JL. A numerical study of laminar forced convection in sinusoidal ducts with arc lower boundaries under uniform wall temperature. Numerical Heat Transfer: Part A: Applications. 2001 Jul 1;40(1):55-72.

[58]. Rezk AR. Theoretical and experimental investigation of silica gel/water adsorption refrigeration systems (Doctoral dissertation, University of Birmingham), 2012.

[59]. Alam KA, Saha BB, Akisawa A. Adsorption cooling driven by solar collector: a case study for Tokyo solar data. Applied Thermal Engineering. 2013 Feb 1;50(2):1603-9.

[60]. Abdel-Salam M, Zaidi A, Cable M. Field study of heating performance of three ground-source heat pumps in Canadian single-family houses. Energy and Buildings. 2021 Sep 15;247:110959.

Appendix

The dependency of the solution from the time step for Chapter two's simulations is studied. Time step 0.01 (s) is chosen. Figure A1 shows the result for an outside temperature of -10 °C for with fan and without fan simulations when the time step is 0.01s. Figure A2 shows the result for an outside temperature of -10 °C for with fan and without fan simulations with a time step of 0.02 s.

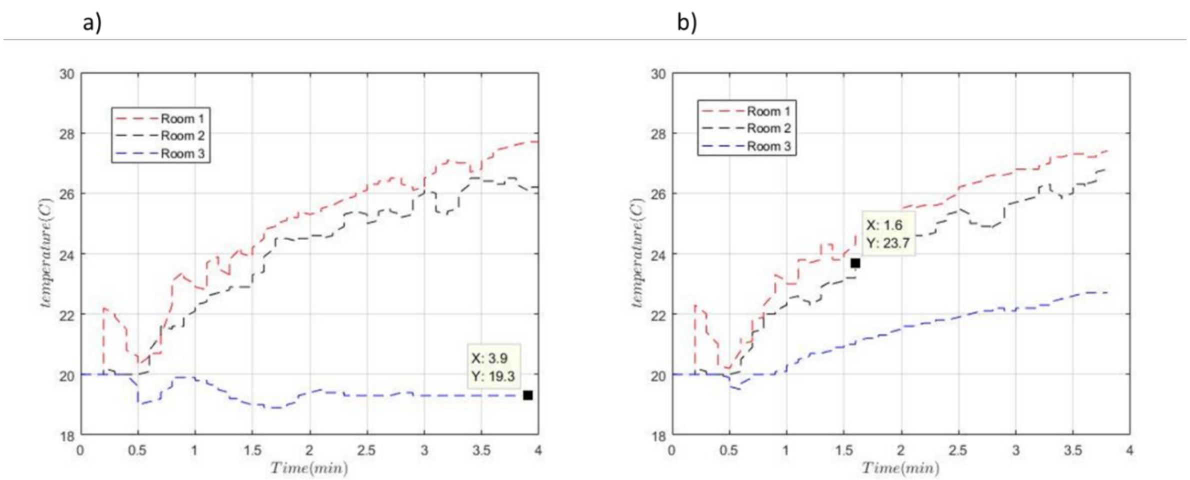

Figure A1. Simulation results for an outside temperature of -10 °C with time step 0.01 (s), (a) with fan, (b) without fan.

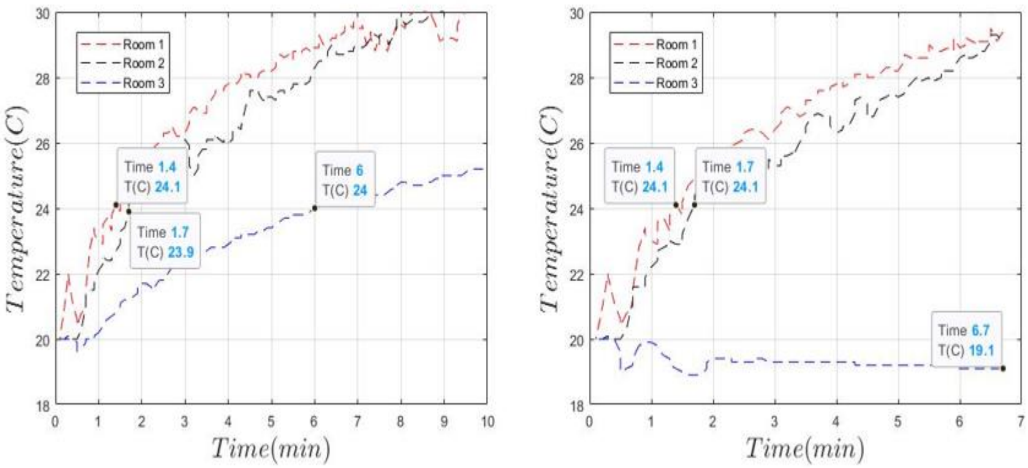

Figure A 2. Simulation results for an outside temperature of -10 °C with time step 0.02 (s), (a) with fan, (b) without fan.

Simulations were performed to investigate the dependency of the solution on the grid parameters for the simulations performed in Chapter Three. Figure A3 shows simulation results when the mesh size is 119,411 elements for heating and cooling under an outside temperature of 5 °C with both fan and dampers installed (condition 4). Figure A4 shows simulation results when 82,825 elements were used for heating and cooling under an outside temperature of 5 °C with both fan and dampers installed (condition 4).

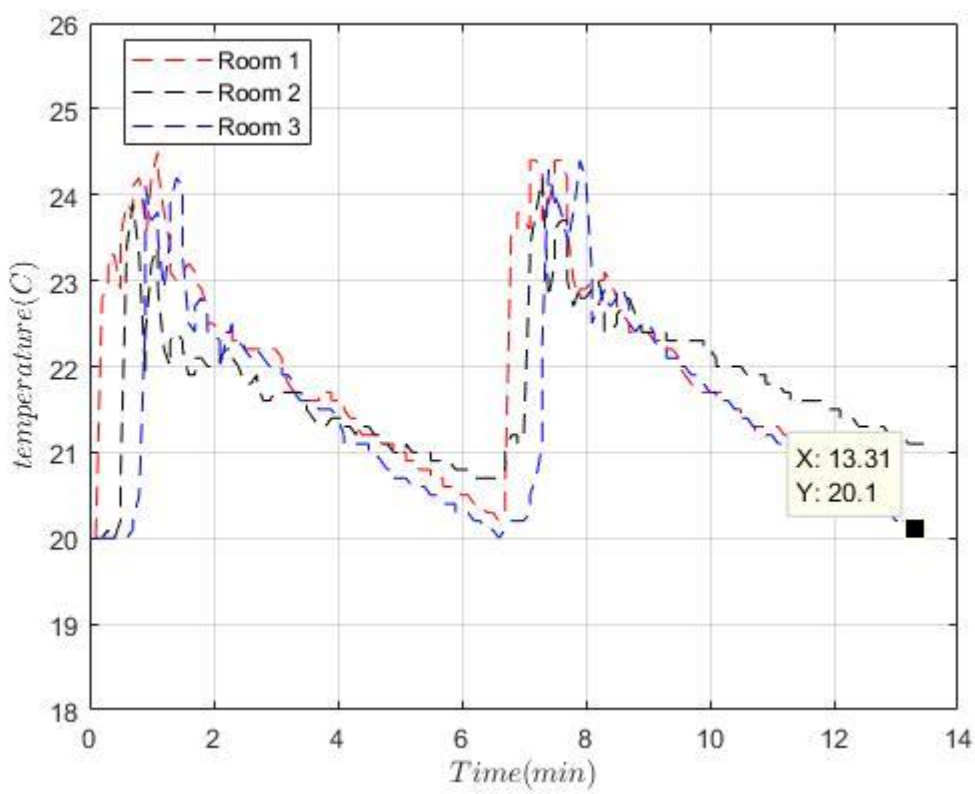

Figure A3. Simulation results for heating and cooling under an outside temperature of 5 °C with both fan and dampers installed (condition 4) with 119,411 elements.

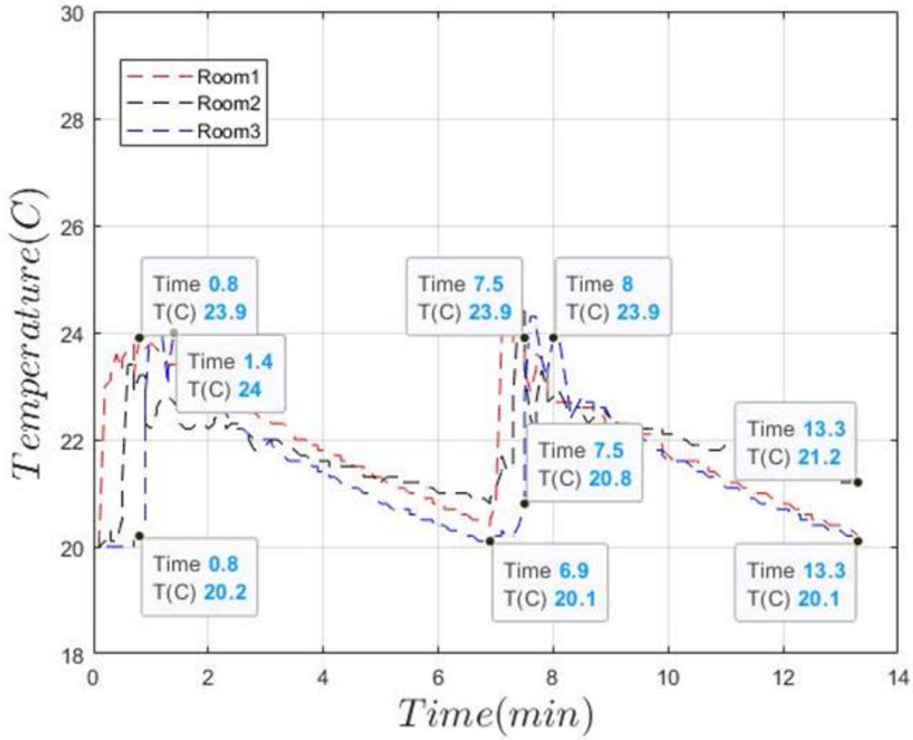

Figure A 4. Simulation results for heating and cooling under an outside temperature of 5 °C with both fan and dampers installed (condition 4) with 82,825 elements.

The dependency of the solution on the mesh parameters used for all cases simulated in Chapter Three were studied. The mesh properties for a second set of simulations for determining the heat transfer within channels are given in Table A1. The mesh properties used in the simulations that gave the results reported in Chapter Three for determining the heat transfer within channels are given in Table A2.

Table A1. Mesh properties used in a second set of simulations for the channels to check the dependency of the solution on the grid.

Shape	Min size (m)	Aspect ratio	Skewness	Growth rate	Number of elements
Circular	$1.46*10^{-5}$	2.2	0.249	1.2	6554
Triangular	$1.46*10^{-5}$	4.6	0.166	1.2	9432
Rectangular	$1.46*10^{-5}$	3.8	0.003	1.2	9504
Sinusoidal	$1.46*10^{-5}$	3.5	0.180	1.2	257550

Table A2. Mesh properties used in the simulations for the results given in Chapter Three for the channels.

Shape	Min size (m)	Aspect ratio	Skewness	Growth rate	Number of elements
Circular	$1.46*10^{-5}$	1.64	0.240	1.2	4536
Triangular	$1.46*10^{-5}$	3.9	0.183	1.2	6768
Rectangular	$1.46*10^{-5}$	3.1	0.003	1.2	6390
Sinusoidal	$1.46*10^{-5}$	3.2	0.150	1.2	298240

The new mesh properties used in the simulations for determining the heat transfer within beds are given in Table A3. The mesh properties used in the simulations in Chapter Three for determining the heat transfer within beds are given in Table A4.

Table A3. Mesh properties used in a second set of simulations for the beds to check the dependency of the solution on the grid.

Shape	Min size (m)	Aspect ratio	Skewness	Growth rate	Number of elements
Sinusoidal	$1.46*10^{-5}$	1.54	0.347	1.2	705936
Triangular 1	$1.46*10^{-5}$	2.8	0.184	1.2	17952
Triangular 2	$1.46*10^{-5}$	3.0	0.187	1.2	18720
Rectangular 1	$1.46*10^{-5}$	3.17	0.017	1.2	18095
Rectangular 2	$1.46*10^{-5}$	3.59	0.022	1.2	17346

Table A4. Mesh properties used in the simulations for the results given in Chapter Three for the beds.

Shape	Min size (m)	Aspect ratio	Skewness	Growth rate	Number of elements
Sinusoidal	$1.46*10^{-5}$	1.68	0.342	1.2	575865
Triangular 1	$1.46*10^{-5}$	2.3	0.177	1.2	14740
Triangular 2	$1.46*10^{-5}$	2.5	0.180	1.2	15600
Rectangular1	$1.46*10^{-5}$	2.25	0.019	1.2	12420
Rectangular 2	$1.46*10^{-5}$	2.56	0.015	1.2	11890

Figure A5 shows the average outlet temperature for the four different channel shapes when the mesh parameters given in Table A1 are used. Figure A6 shows the average outlet temperature for the four different channel shapes reported in Chapter Three, which were simulated using the mesh parameters given in Table A2.

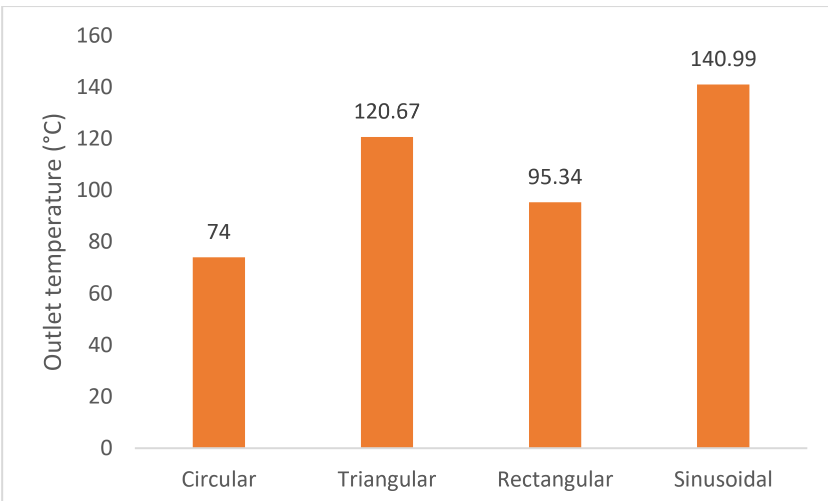

Figure A5. Average outlet temperature for different channel shapes for checking the dependency of the solution on the grid (simulated using the mesh parameters in Table A1).

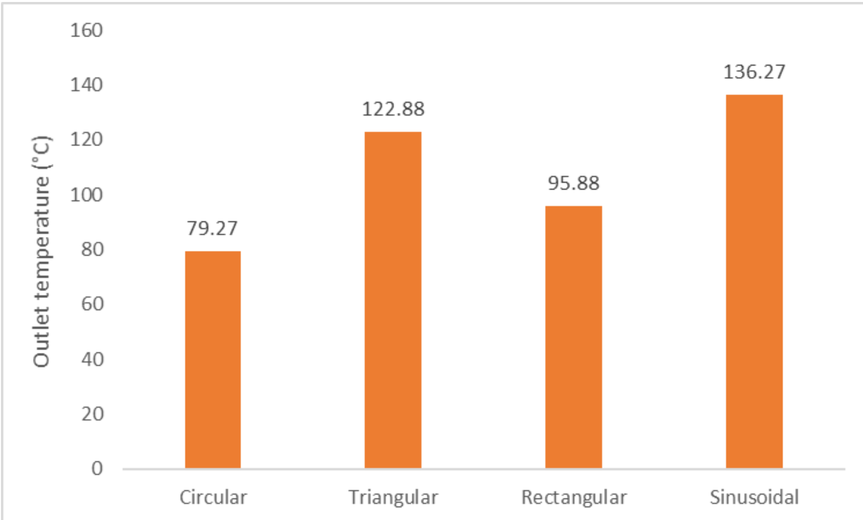

Figure A6. Average outlet temperature for different channel shapes (simulated using the mesh parameters in Table A2).

Figure A7 shows the average outlet temperature for the four different bed shapes when the simulations are performed using the mesh parameters in Table A3. Figure A8 shows the average outlet temperature for the four different bed shapes reported in Chapter Three, which were simulated using the mesh parameters in Table A4.

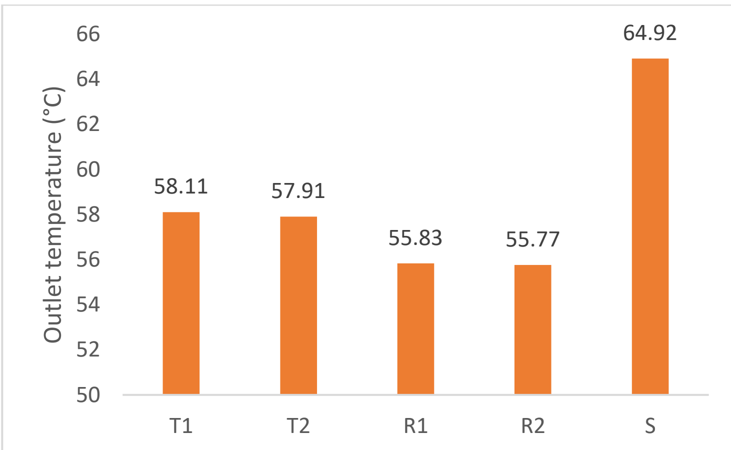

Figure A7. Average outlet temperature for different bed shapes simulated to check the dependency of the solution on the grid (simulated using the mesh parameters in Table A3).

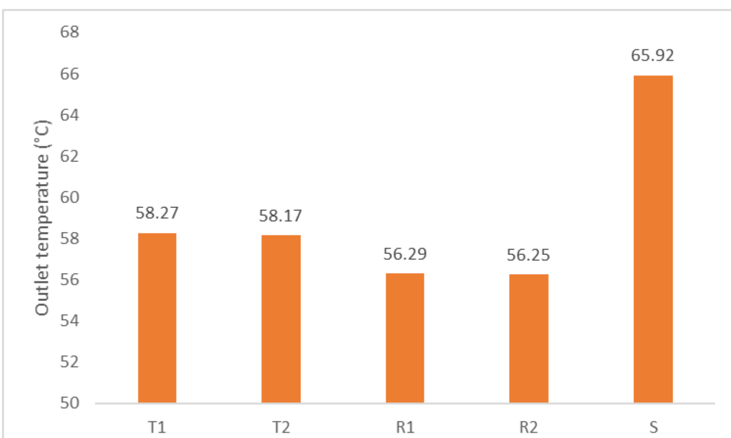

Figure A8. Average outlet temperature for different bed shapes (simulated using the mesh parameters in Table A4).

Figures A9 to A14 show the second and third experimental results of discharging processes with air velocities 0.4, 0.6, 0.8 m/s.

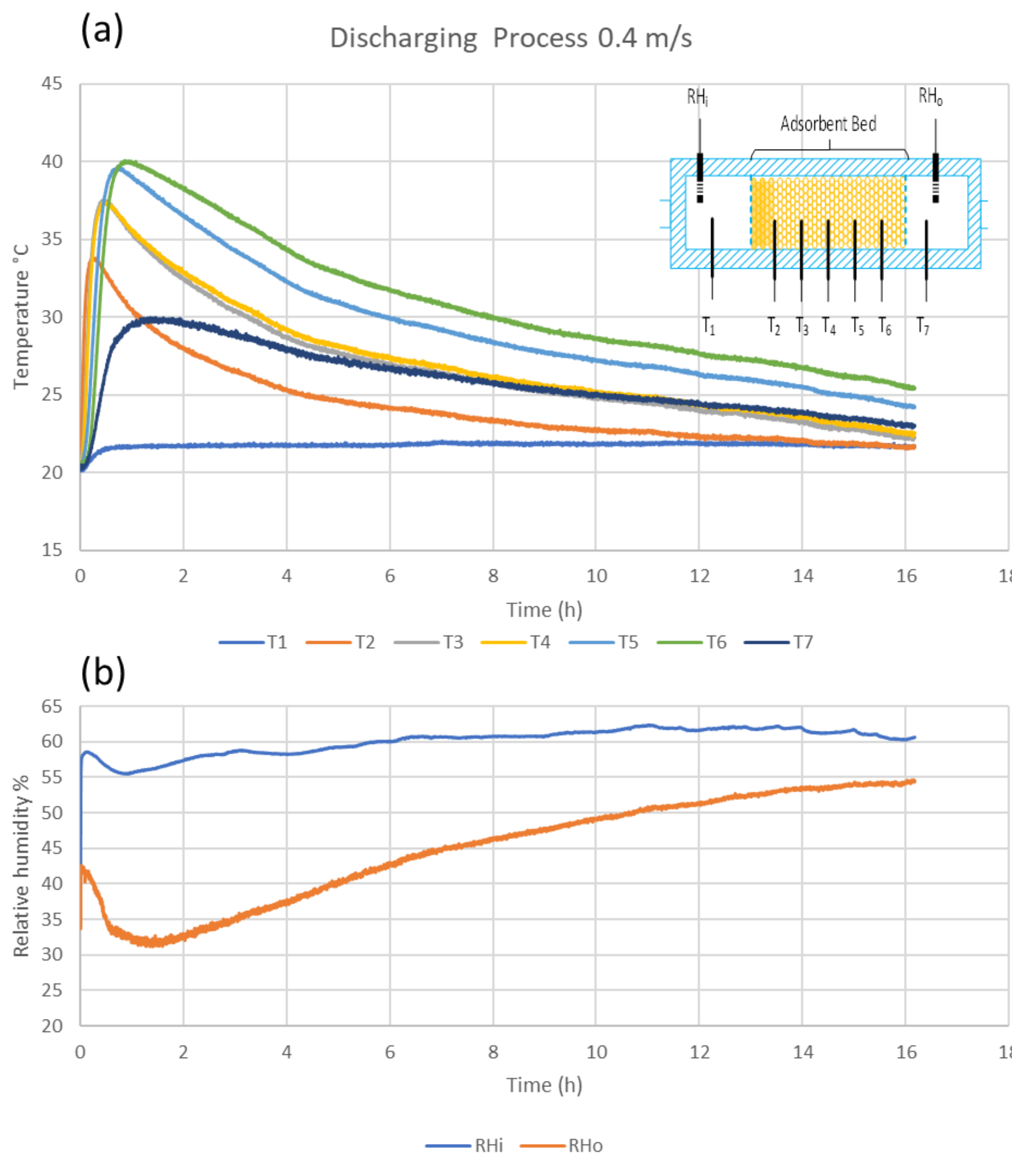

.

Figure A9. Experimental results for the second experiment of the discharging process at an air velocity of 0.4 m/s (a) Temperatures (b) Relative humidity.

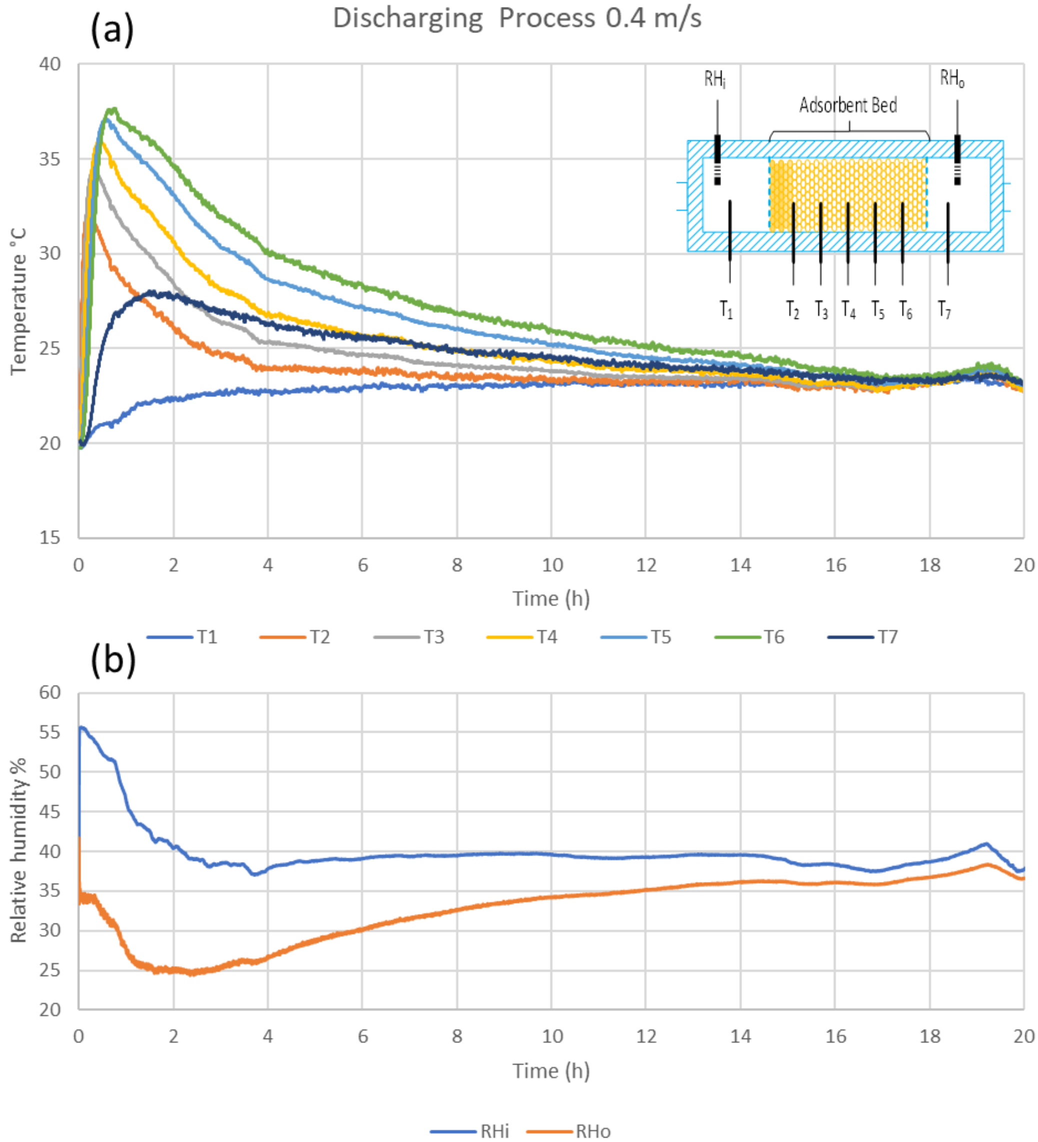

Figure A10. Experimental results for the third experiment of the discharging process at an air velocity of 0.4 m/s (a) Temperatures (b) Relative humidity.

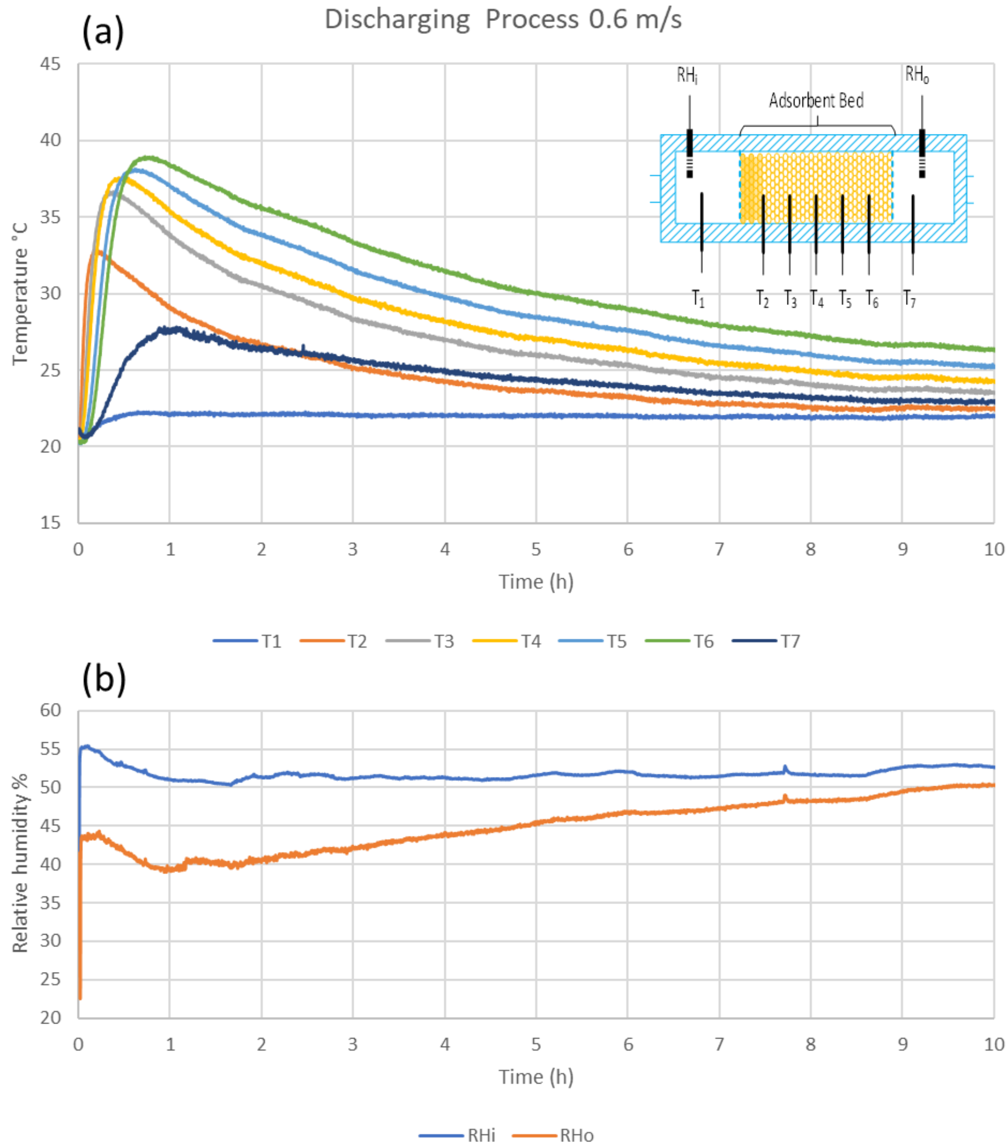

Figure A11. Experimental results for the second experiment of the discharging process at an air velocity of 0.6 m/s (a) Temperatures (b) Relative humidity.

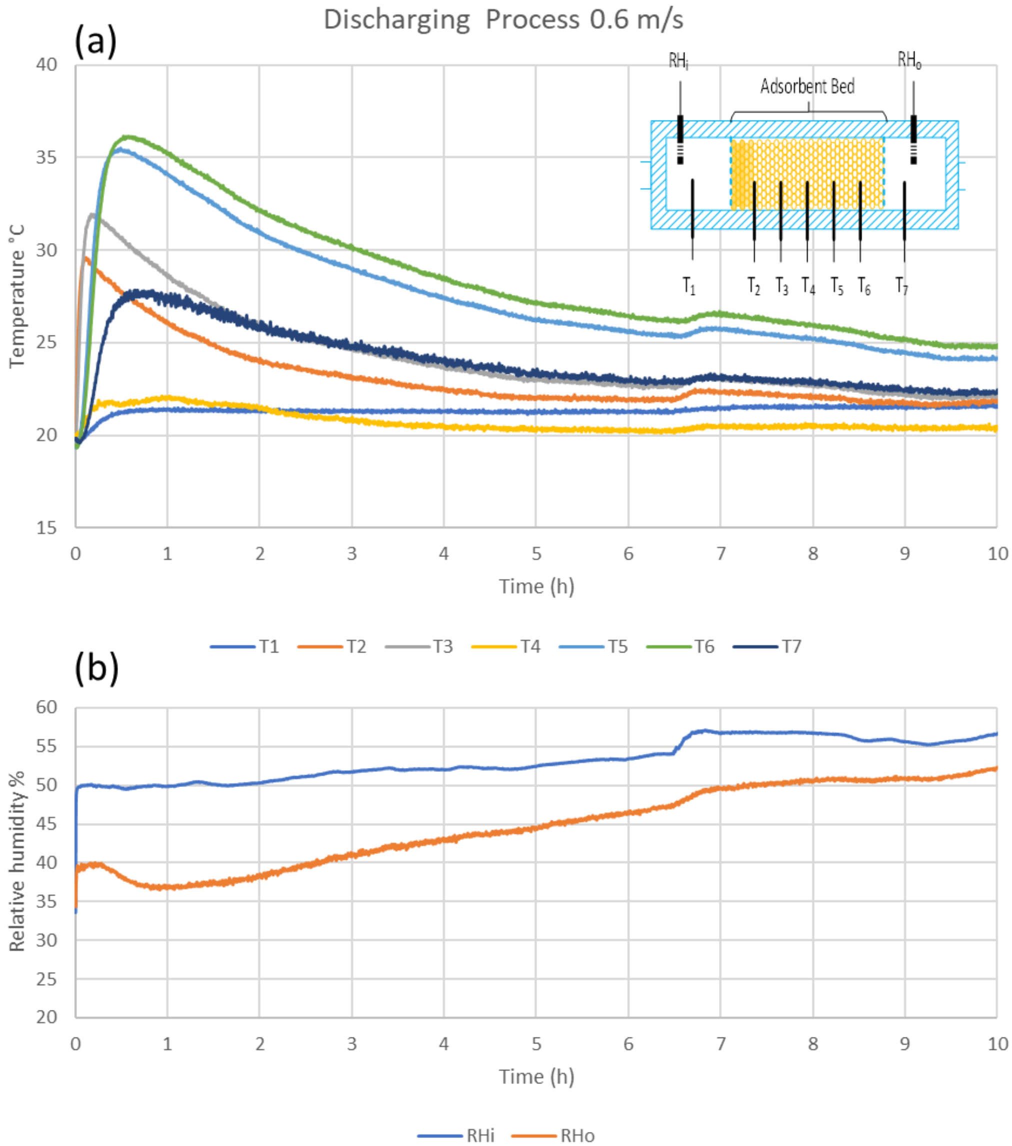

Figure A12. Experimental results for the third experiment of the discharging process at an air velocity of 0.6 m/s (a) Temperatures (b) Relative humidity.

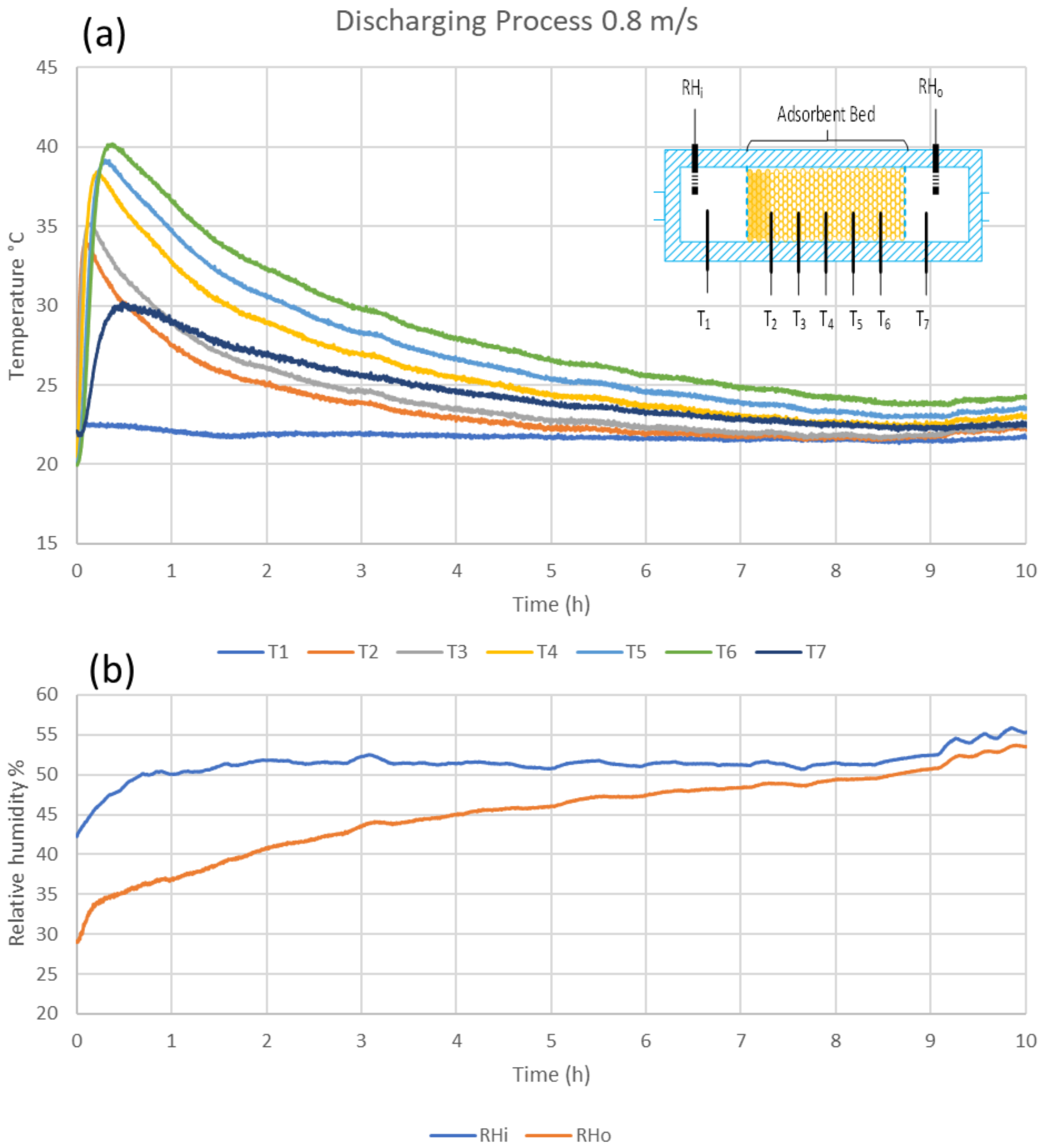

Figure A13. Experimental results for the second experiment of the discharging process at an air velocity of 0.8 m/s (a) Temperatures (b) Relative humidity.

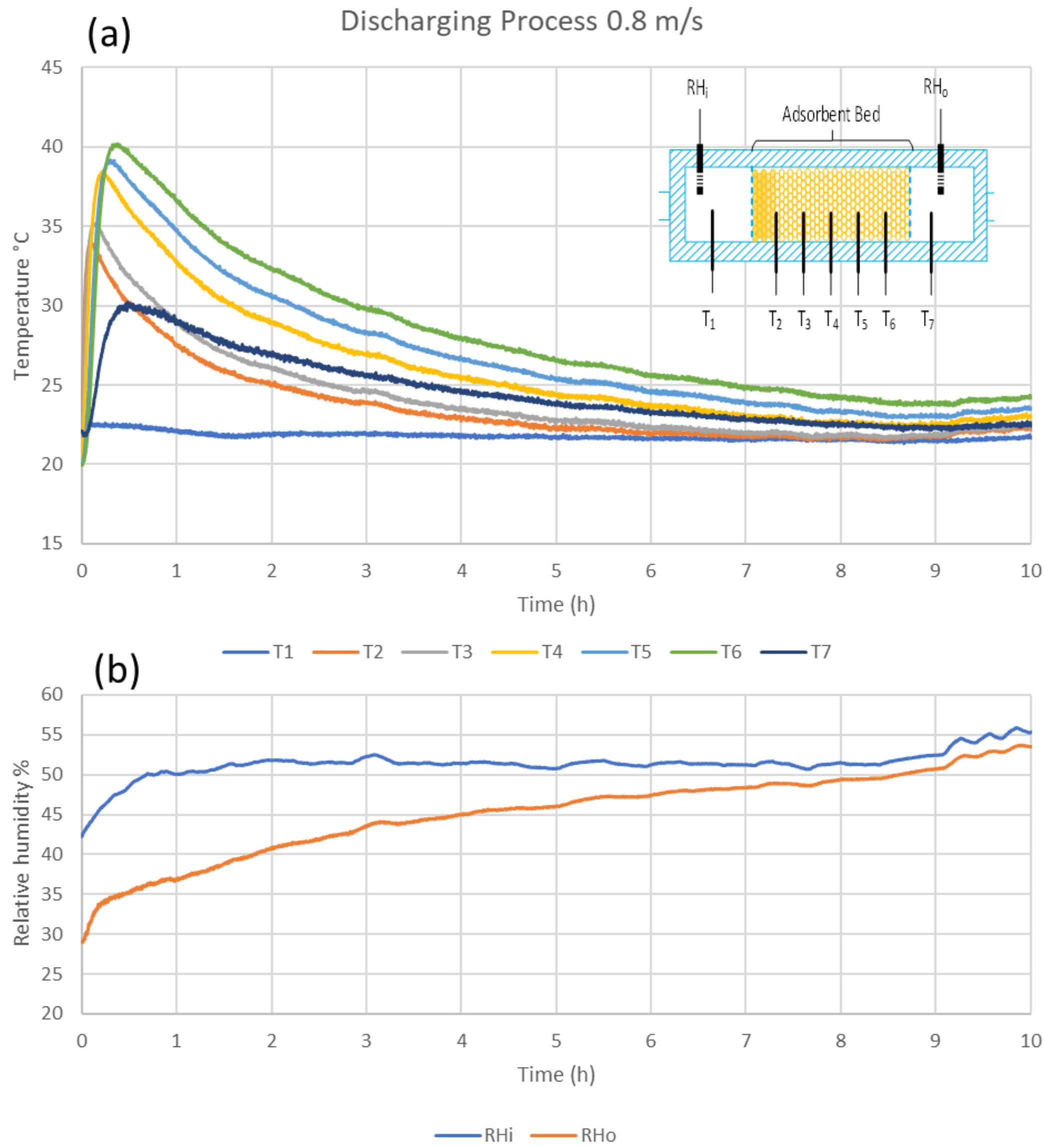

Figure A14. Experimental results for the third experiment of the discharging process at an air velocity of 0.8 m/s (a) Temperatures (b) Relative humidity.